INTERACTIONS OF ELECTROMAGNETIC WAVES WITH MICRO/NANO PARTICLES: MANIPULATION AND CHARACTERIZATION

by

Dongxiao Li

B.S. in Physics, Fudan University, 2002

M.S. in Optical Science and Engineering, Fudan University, 2005

Submitted to the Graduate Faculty of

Swanson School of Engineering in partial fulfillment

of the requirements for the degree of

Doctor of Philosophy

University of Pittsburgh

2011

UNIVERSITY OF PITTSBURGH

SWANSON SCHOOL OF ENGINEERING

This dissertation was presented

by

Dongxiao Li

It was defended on

Mar. 25th, 2011

and approved by

Joel Falk, Professor, Department of Electrical and Computer Engineering

William Stanchina, Professor, Department of Electrical and Computer Engineering

Guangyong Li, Assistant Professor, Department of Electrical and Computer Engineering

Sanford H. Leuba, Associate Professor, Department of Cell Biology and Physiology

Dissertation Director: Hong Koo Kim, Professor, Department of Electrical and Computer Engineering

INTERACTIONS OF ELECTROMAGNETIC WAVES WITH MICRO/NANO PARTICLES: MANIPULATION AND CHARACTERIZATION

Dongxiao Li, PhD

University of Pittsburgh, 2011

Interaction of electromagnetic waves with small particles has been extensively investigated for detection, characterization and manipulation of objects in the micro/nanoscale. Several advanced techniques based on light-particle interaction have been developed and widely used in biomedical research, e.g., trapping of micron-size particles by light and plasmonic photothermal therapy with gold nanoparticles.

In this thesis we have developed two new methods of optical trapping by use of planar metal nano-optic structures. One is based on a metallic nanoslit array structure that is designed to allow refractive transmission of light with proper phase retardation at each slit, shaping an incident light into a sharp focus. The metallic nanoslit array lenses were integrated with a fluidic channel cell, and optical trapping of polystyrene microspheres was demonstrated. Another optical trapping method developed in this thesis utilizes the diffraction phenomenon occurring at a thin-film metal edge. Interference of boundary diffraction and free-space transmission waves is found to generate highly localized distribution of light around the metal edge. The electromagnetic field distribution around the edge was calculated by finite-difference-time-domain method, and the 2D trapping forces were estimated by applying a ray optics model. Trapping of a 2-μm-diameter polystyrene bead was demonstrated, and the trapping force (escape force) is measured to be about 2.2 pN at incident power of 32 mW. Selective trapping and sorting of microspheres by this metal edge trapping is also demonstrated.

Use of metal nanoparticle colloidal solutions in conjunction with radiofrequency (RF) waves has recently drawn attention as a possible means to deposit heat in a local confined space for cancer therapy. We investigated the heating effect of gold nanoparticle (Au-NP) colloids in the presence of RF electromagnetic wave, and explored the possible role of Au-NPs in RF energy absorption. Contrary to the previously-taken assumption in this field, we found that Au nanoparticles do not contribute to RF energy absorption. Au-NPs were physically separated from the colloidal solutions via centrifugation, and RF heating and electrical conductivity measurements were performed. The results show that the dominant mechanism of RF-radiation-to-thermal conversion is due to the Joule heating via ionic conduction in the electrolyte solutions.

TABLE OF CONTENTS

LIST OF FIGURES

PREFACE

This thesis is based on the studies conducted during August 2005 to March 2011 at the Department of Electrical and Computer Engineering, University of Pittsburgh.

I would like to use this opportunity to thank the following people that have made this thesis possible. First, I would like to express my sincere gratitude to my advisor, Dr. Hong Koo Kim. This thesis would never have come to a reality without his advice, unique support, encouragement, and inspiration throughout my doctoral program.

I would like to thank the members of my dissertation committee, Dr. Joel Falk, Dr. William Stanchina, Dr. Guangyong Li at the Department of Electrical and Computer Engineering, Dr. Sanford Leuba at the Department of Cell Biology and Physiology, and Dr. Susan Gilbert, who was at the Department of Biological Sciences of the University of Pittsburgh and is now at the Rensselaer Polytechnique Institute, for their taking time to serve on my committee and giving me invaluable comments and suggestions on this thesis. Especially Dr. Gilbert kindly taught me how to process microtubules in the early stage of my thesis research.

Moreover, I would like to thank my colleague, Yun Suk Jung for his help in experiments and many discussions on sample fabrication, and Yonggang Xi for his help in FDTD simulation and optical trapping force calculation.

Most of all I would like to express my greatest thanks to parents and my sisters, who have always believed in me and supported me during my studies. Finally, my gratitude goes to my boyfriend Yonggang Xi again, for his love and companionship that support me all along the way.

1.0 INTRODUCTION

The interaction of electromagnetic wave with small particles has been extensively studied over the past centuries and has a venerable history. Light microscopy, using light to detect/observe small particles, involves the diffraction, reflection, or refraction of electromagnetic waves interacting with the specimen, and the subsequent collection of this scattered radiation or another signal in order to create an image. Light wave is one of the important tools in biological research. Living cells are typically 10 μm across. The cell parts such as nucleolus and microtubules are much smaller and are in the sub-micron size domain. Proteins are smaller with a typical size of just 5 nm. Knowledge of optical interactions of biological materials is important in characterizing biological materials and processes. The understanding of how electromagnetic waves interact with micro/nanometer-sized objects also has enabled several advanced techniques, e.g., microscopic imaging, fluorescent biological labels, optical trapping [1,2,3,4,5,6] and thermotherapy by light-simulated metal nanoparticles [7, 8, 9, 10, 11]. These techniques are widely used in biological research and have made great impacts in biology and life sciences.

Optical trapping has become an essential technique to handle/manipulate micron-size objects. It can immobilize, manipulate or transport micron-size objects in a non-contact fashion in microscale environment. As microfluidic and lab-on-a-chip devices become a trend in small-analyte-amount assays and biological applications, novel miniaturized optical lenses are drawing increasing attention for use in optical trapping.

A field that has shown fast growth over the past decades is the use of nanoparticles in biology, or life sciences. Nanoparticles becomes widely used because their size is much smaller than cells and can be used as very small probes that would allow us to spy at the cellular machinery without introducing too much interference. In recent years, heat generation by metal nanoparticles under electromagnetic radiation has also attracted much interest [7, 8, 9, 10, 11, 12, 13, 14, 15, 16,17,18,19, 20]. Metal nanoparticles can efficiently generate heat when electromagnetic radiation of proper wavelength is applied. The heating process becomes strongly enhanced at plasmon resonance. The heating efficiency can be adjusted by the size, shape and organization of the nanoparticles. Heating by light-simulated metal nanoparticles has been used for many applications such as biomedicine imaging [8], cancer treatment [7, 10] and drug release [20].

In this thesis, we have developed novel planar optical trapping structures, which are easy to implement and also offer advantage in integration with microfluidic system. One is based on a metallic nanoslit array structure, which can shape an optical beam by properly designed phase retardation at each slit element. Another is optical trapping by a metal edge structure, which enables trapping function via diffraction and interference of incident light around the metal corner.

We also investigated the heating effect of gold nanoparticle colloids in the presence of radiofrequency (RF) electromagnetic wave. Also investigated in this study is the possible role of Au NPs in RF energy absorption in the gold colloidal solutions [21, 22, 23, 24].

1.1 MANIPULATION OF DIELETRIC MICROPARTICLES BY LIGHT

1.1.1 Optical trapping

When a light wave strikes on an object, if the frequency of the light does not match the resonant frequency of vibration of the electron, the light will be only reflected, refracted by or transmit through the object. The momentum transfer associated with bending light gives rise to a force acting on the object. The optical force rises from the momentum change of photons and is traditionally divided into two components: scattering force and gradient force. The gradient force is responsible for optical trapping. Optical force is sensitive to the geometry of objects so that force calculations are mostly carried out on spherical objects. When the diameter of a spherical object is much smaller than the trapping wavelength, a condition referred to as the Rayleigh regime, a dipole model can be used to compute the force. When the object's diameter is much greater than the trapping wavelength, a condition referred to as the Mie regime, a ray optics model is usually used to calculate the force.

Optical trapping has become an essential instrument to manipulate microscopic objects as small as 10 nm. In most biological assays with optical traps, the trapped object is a micron-sized polystyrene or glass bead which is bio-chemically attached to a biological specimen, serving as a "handle" for the optical traps to grab. Displacement of the bead in the focal plane can be tracked with nanometer and millisecond resolution by position detection techniques, and thus the force can be calculated. These optical trap instruments can measure forces on the order of 1 to 100 pN. Well-calibrated optical traps have been developed to measure the properties of DNA [25], step movements of motor proteins [26, 27] and biophysical forces of microtubules [28, 29].

1.1.2 Optical trapping force calculation

Optical traps are based on the radiation pressure, which is a force per unit area on an object due to the momentum change of incident photons. For a light of specific wavelength λ, the momentum carried by a single photon is $p = \frac{h}{\lambda}$. As an incident light strikes on a dielectric object whose refractive index is greater than the surrounding environment, the light is scattered into a wide range of directions. The net force $\vec{F}$ due to the momentum change of the incident photons is given by the difference between the momentum flux entering the object ($\vec{S}_{in}$)and that leaving the object ($\vec{S}_{out}$), and is expressed as below:

$$\vec{F} = \frac{n}{c}\iint_{S}(\vec{S}_{in} - \vec{S}_{out})dA\,. \tag{1}$$

where n is the refractive index of the dielectric object, c is the speed of light in vacuum, s is the boundary surface of the object, and dA is an element of area normal to the Poynting vector. The force has been traditionally divided into two components: scattering force and gradient force. The scattering force is proportional to the light intensity and pushes the object in the direction of the light. However, optical traps owe their trapping to the gradient force which is proportional to both the polarizability of the light and the spatial gradient of the field. The gradient force arises from the fact that induced dipole in an inhomogeneous external electric field experiences forces directing to the gradient of the field. For an isotropic scatterer, the resulting net force is canceled except in the forward direction. In most conventional cases, the scattering dominates and an

effective scattering cross section can be calculated for the object. However, if the light gradient is steep, the gradient force cannot be neglected.

Most of the theoretical models deal only with spherical dielectrics and are limited to two regimes. When the spherical particle is much smaller than the wavelength of the light, the Rayleigh scattering condition is satisfied. In this regime, a dipole model treats the particle as a dipole with an external instantaneous electric field uniform over the whole particle extent. The dipole momentum is given by [6, 30]:

$$p(r,t) = 4\pi n_m^2 \varepsilon_0 a^3 \left(\frac{m^2 - 1}{m^2 + 2} \right) E(r,t) . \tag{2}$$

where n_m and n_p is the refractive index of surrounding material and the particle respectively, $m = n_p / n_m$ is the relative index of the particle and a is its radius. The induced point dipole follows synchronously the harmonic oscillation of the electric field and radiates secondary or scattered waves in all directions. This scattering force acting on the dipole induced by the electromagnetic field is given by

$$F_{scat}(r,t) = \frac{n_m}{c} \sigma I_0 . \tag{3}$$

$$\sigma = \frac{8}{3} \pi (ka)^4 a^2 \left(\frac{m^2 - 1}{m^2 + 2} \right)^2 . \tag{4}$$

where σ is the scattering cross section of the particle and $k = 2\pi n_m / \lambda$ is the wavelength number of the incident light.

The gradient force is given by:

$$F_{grad}(r,t) = [\,p(r,t)\cdot\nabla]E(r,t) = 4\pi n_m^2 \varepsilon_0 a^3 \left(\frac{m^2-1}{m^2+2}\right)\frac{1}{2}\nabla E^2(r,t)\,. \tag{5}$$

Then the time-average gradient force on a dipole is given by:

$$F_{grad}(r) = < F_{grad}(r,t) >_T = 4\pi n_m^2 \varepsilon_0 a^3 \left(\frac{m^2-1}{m^2+2}\right)\frac{1}{2}\nabla < E^2(r,t) >_T\,. \tag{6}$$

$$= \frac{2\pi n_m a^3}{c}\left(\frac{m^2-1}{m^2+2}\right)\nabla I(r)\,. \tag{7}$$

The gradient force is proportional to the gradient of the light intensity and points in the direction of the gradient when the refractive index of the particle is greater than the surrounding medium (m > 0).

Where the radius of the sphere is much larger than the wavelength of the trapping laser (Mie regime), a dipole model is no longer valid. In this regime, diffraction is neglected and ray optics (RO) method is applied to calculate the force. In the ray optics the total light beam is decomposed into individual rays and each has appropriate intensity, direction, and state of polarization. Figure 1 illustrates the traditional ray-optics diagram used to qualitatively describe the trapping forces acting on a spherical dielectric particle [2]. Parallel rays entering the back focal plane of an objective converges into a diffraction-limited spot on the surface of a dielectric sphere. The reflected and refracted rays give rise to optical forces. Based on the Fresnel formulas, for a single beam incident with a θ angle, the resulting force can be divided into two

components, scattering force and gradient force, which are parallel and perpendicular to the incident ray respectively, and are given by Ashkin in 1992 [2]:

$$F_{scat} = \left\{1 + R\cos 2\theta - \frac{T^2[\cos(2\theta - 2\alpha) + R\cos 2\theta]}{1 + R^2 + 2R\cos 2\alpha}\right\}\frac{n_m P}{c} = Q_s \frac{n_m P}{c}. \quad (8)$$

$$F_{grad} = \left\{R\sin 2\theta - \frac{T^2[\sin(2\theta - 2\alpha) + R\sin 2\theta]}{1 + R^2 + 2R\cos 2\alpha}\right\}\frac{n_m P}{c} = Q_g \frac{n_m P}{c}. \quad (9)$$

where θ is the incident angle and α is the refractive angle. T and R are the Fresnel transmission and reflection coefficients and Q_s and Q_g are the scattering and gradient efficiencies.

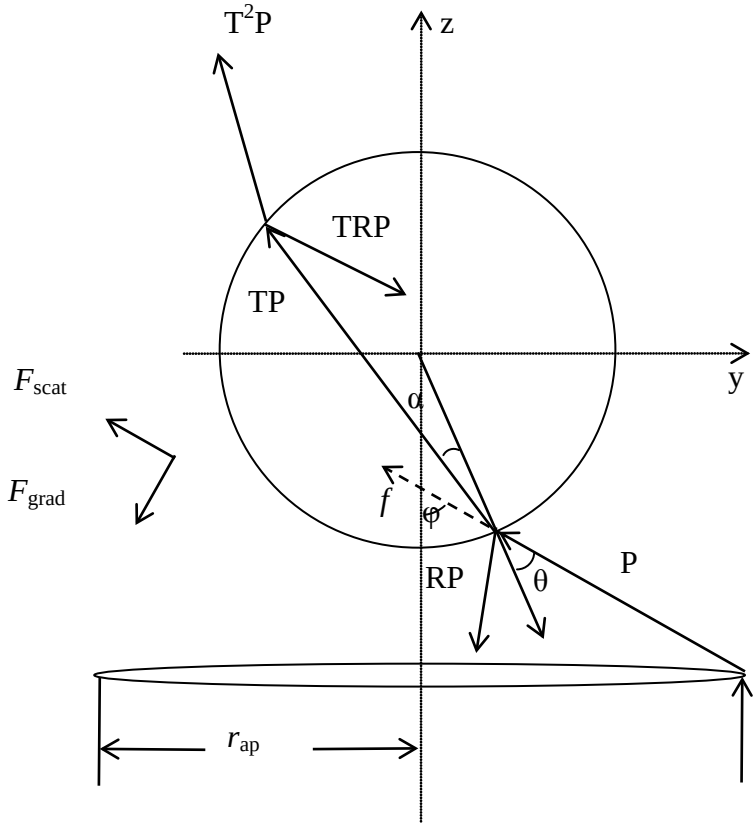

Figure 1. Ray-optics diagram of a single beam trap. A single incident beam of power P strikes on the surface of a dielectric particle at an incident angle of θ, giving rise to successively reflected and refracted rays of decreasing power RP, TP, T^2P, TRP, etc. the total force is the contribution of all these rays and can be divided into two components: scattering force gradient force which parallel and perpendicular to incident direction, respectively [2].

In the –z direction, the total force is the smallest. To trap an object in this direction, the gradient forces must be larger than the scattering force. The RO theory predicts that the rays with large incident angle contribute more portions to the gradient force than the center rays. Therefore, a stronger trap can be formed by using a high N.A. objective and expending incident beam to overfill the back aperture of the objective.

When the particle size is intermediate, i.e., its radius is comparable to the wavelength, neither of the RO and EM approaches is accurate. More complete EM theories are required to accurately describe the model. The calculation usually becomes practically intractable and is difficult to compare with the experiment [4]. In most biological applications, the radius of the beads used often varies from 0.1-10 μm, which is comparable to the trapping wavelength (1064 nm or 980 nm laser are mostly used as trapping light in order to reduce the bio-damage). In these cases, diffraction cannot be neglected and neither of the RO theory nor dipole model is applicable. The i component of the time-average force due to the electromagnetic field can be obtained by the integral of the Maxwell stress tensors T_{ij} over the surface enclosing the particle [30]:

$$F_i = \left\langle \oint_S T_{ij} n_j da \right\rangle . \tag{10}$$

$$T_{ij} = \frac{1}{4\pi}\left[\varepsilon E_i E_j + B_i B_j - \frac{1}{2}(\varepsilon E_i E_i + B_i B_i)\delta_{ij} \right]. \tag{11}$$

where n_j is the outward unit normal vector and ε is the electric permittivity. However, it is difficult to calculate each term in the bracket. Considerable work has been done to predict the trapping force in this regime and a brief review is given by Ref [5].

1.1.3 Optical trapping instrument and characterization

Optical forces are sensitive to the perturbation in geometry. In most cases, theoretical models cannot quantitatively predict the force. Thus in practice, an optical trap must be calibrated before the instrument can be used.

The hydrodynamic drag-force approach is the most common method to measure the escape force (the maximal transverse trapping force). Figure 2 shows the schemes for force calibration by the drag force method in a flow cell. In a flow cell, the hydrodynamic drag force experienced by a stationary bead can be calculated by:

$$F = -\beta v . \tag{12}$$

where β is the viscous drag coefficient and v is the flow velocity at the center of the bead. For a sphere of radius a, β is given from the modified Stokes's theorem [5, 31]:

$$\beta = \frac{6\pi a \eta}{1 - \frac{9}{16}(\frac{a}{h}) + \frac{1}{8}(\frac{a}{h})^3 - \frac{45}{256}(\frac{a}{h})^4 - \frac{1}{16}(\frac{a}{h})^5} . \tag{13}$$

where η is the fluidic viscosity and h is the distance between the center of bead and wall. Under the flow, the bead was pushed away y distance from optical potential center, the trapping force is determined by x and the stiffness of the trap k and can be express as:

$$F_t = -kx . \tag{14}$$

The negative sign implies that the trapping force tends to pull the object back to the trap center. When the drag force increases and at the point that it is exactly equal to the maximum trapping force that the edge trap can provide, the bead escaped by thermal motion. By taking a video of the entire escape process, the local fluid velocity is then measured by tracking beads immediately after leaving the trap, or by monitoring other beads in the flow field in the same focus plane.

The escape force describes the strength of an optical trap, however, the relationship between the force and the displacement of the object from the trap center, i.e. trap stiffness should be determined before the instrument can be used as a force detector. This includes position and force calibration. Two parameters, position detector sensitivity and trap stiffness constant, have to be determined in order to calculate the trapping force. The accuracy of measurement of these parameters is the heart of the quantitative performance of optical trapping.

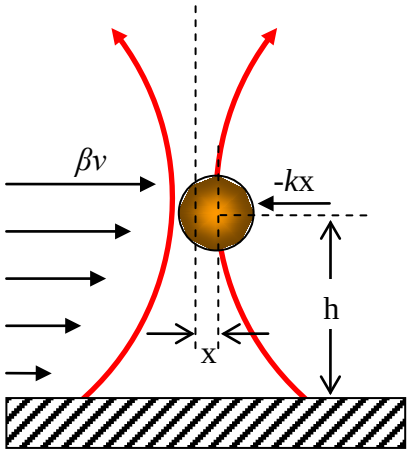

Figure 2. Schematic for force calibration by the drag-force method. A laser beam enters from below through a transparent glass slide (wall). The distance between the center of focused laser beam and the wall is h. The bead and the flow cell are assumed to be held stationary when the velocity of the fluid flow increases. The fluid drag force is balanced by the trapping force. The transverse position of the bead respect to the beam center is x.

In the position calibration, the relation between the displacement of the particle and the corresponding sensor output voltage is quantitatively determined. A quadrant-photodiode detector (QPD) which is a 2×2 array of individual photodiode active areas, separated by a small gap, fabricated on a single chip, is used most frequently for the position detector in optical trapping instrument [32]. Usually a particle is fixed on the substrate of the specimen chamber and the image of the particle is focused on the center of a QPD which gives a null voltage. Then the chamber moves at a constant spend relative to the objective. When the displacement of the image of the particle from the center of the QPD (x) increases, the output voltage (V) changes. The detector signal is linear for beam displacements within the detector linear response region and is expressed as:

$$x = \beta V \, . \tag{15}$$

where inversion of the slope β (in V/μm) is defined as the sensitivity of the position detector and will be used in the force calibration.

Instead of measuring the trapping force directly, the stiffness constant is determined for calculation for the force. For small displacement of the particle from its equilibrium position, the drawing force, named as gradient restoring force, is simply proportional to the displacements. In other words, the optical trap acts as a Hooke's spring and can be described by the equation:

$$\vec{F} = -k\vec{x} \, . \tag{16}$$

where k is the stiffness of the linear spring, and $\vec{x}$ is the radial displacement. The knowledge of the parameters of β and k is sufficient for calculation the trapping force.

Several different methods of stiffness calibration are implemented. Among them, power spectrum and equipartition calibration are most often used. The power spectrum calibration is to measure the Brownian motion of trapped particle [33]. Consider a particle of a radius r is trapped in a fluid with a viscous drag γ at the temperature T. The equation of motion is given by:

$$\gamma \frac{dx}{dt} + kx = F(t) . \tag{17}$$

where x is the displacement, k is stiffness of the trap and $F(t)$ is an external driving force. $F(t)$ only due to the thermal fluctuations is random and given as:

$$| F(f) |^2 = 4\gamma k_B T . \tag{18}$$

where k_B is the Boltzmann constant. The solution to Eq.(18) can be obtained by taking Fourier transform of both sides, which is characterized by a Lorentzian power spectrum of $x(t)$:

$$S_x(f) = \left| X(f) \right|^2 = \frac{k_B T}{\gamma \pi^2 (f_c^2 + f^2)} . \tag{19}$$

$$f_c = \frac{k}{2\pi\gamma} . \tag{20}$$

At low frequency, the power spectrum is approximately constant and

$$S_x(f) \approx S_0 = \frac{k_B T}{\gamma \pi^2 f_c^2}. \tag{21}$$

At high frequency, power spectrum decreases proportional to f^{-2}. The transition frequency f_c is the roll-off frequency (or corner frequency).

Using the linear relation of displacement and output voltage $x(t) = \beta V(t)$, the power spectrum of *V(t)* is given by:

$$S_V(f) = |V(f)|^2 = \frac{1}{\beta^2} S_x(f) = \frac{k_B T}{\beta^2 \gamma \pi^2 (f_c^2 + f^2)}. \tag{22}$$

At low frequency,

$$S_V(f) \approx V_0 = \frac{1}{\beta^2} S_0. \tag{23}$$

From Eq.(20) and Eq.(22), two parameters can be obtained:

$$k = 2\pi\gamma f_c. \tag{24}$$

$$\beta = \sqrt{\frac{k_B T}{\gamma \pi^2 f_c^2 V_0}}. \tag{25}$$

An obvious advantage of this method is that the stiffness measurement is independent of the calibration of the position. Therefore, by fitting the power spectrum *V(f)* to a Lorentzian

shape, f_c can be determined. If the viscous drag is computable, stiffness k will be obtained by Eq.(24).

The equipartition theorem method involves measurement of the mean-square displacement of the trapped particles in a harmonic potential. The thermal fluctuation of the particle is described by:

$$\frac{1}{2}k_B T = \frac{1}{2}k < x^2 > . \tag{26}$$

Combined with the position calibration, we obtain

$$\beta = \sqrt{\frac{< x^2 >}{< V^2 >}} = \sqrt{\frac{k_B T}{k < V^2 >}} . \tag{27}$$

$$k = \frac{k_B T}{\beta^2 < V^2 >} . \tag{28}$$

Similar to the power spectrum method, the power spectrum of *V(t)* is first measured and The mean square offset voltage $< V^2 >$ is

$$< V^2 >= 2\pi \int_0^{+\infty} S_V(f) df \ . \tag{29}$$

Therefore using a fully calibrated position detector, the stiffness is calculated by Eq.(28). In this method, the viscous drag is not needed. Each of these methods has its strength and

weakness. Power spectrum method, unlike the other two, does not require a full calibration of the position. However, similar to the drag force method, it depends on the knowledge of viscous drag γ. For a sphere of radius of r, the viscous drag is given by $\gamma = 6\pi\eta r$, where η is the viscosity of the medium. When the particle is near to a surface, the drag is a function of the distance from the surface. The proximity effect cannot be neglected when the radius of the particle is comparable to the distance from the surface, which is most likely happened for a trapped particle in a chamber. Thus viscosity of the liquid, size of the particle, position of the particle with respect to the surface distance from surface must be determined before calculation of the drag. These parameters are not needed in the equipartition method, in which the position sensor has to be completely calibrated instead.

The above discussion is based on mono-dimensional position detection. Actually, the calibration should be done in three dimensions and the string constants are given for the movements in three axes.

Although optical trapping systems are commercially available, many trapping instruments in a lab are homemade, either modified from microscopes or built by integrating of optical components. A scientific optical trapping system can be divided into three parts: trapping, position manipulating and position sensing. An expanded laser beam is incident into the back aperture of an objective and is focused on the particle. The position of the particle is detected by imaging the particle using a video camera mounted on the camera port of the microscope or focusing an image of the particle into a QPD. The most important element is a high N.A. objective (typically 1.2-1.4). Dynamic control of the trap position is achieved by addition of mirrors or prisms into the optical path before the laser beam enter the objective. Video-based position detection has ~5 nm resolution but is limited to video acquisition (typically ~25-120Hz).

High-bandwidth position detection can be achieved by using a QPD, and the typical frequency used is around 1 kHz. Signals of the QPD are captured by a data acquisition card and are stored or processed by a computer. Furthermore, a piezoelectric stage is often used to move the sample chamber relative to the trap, which greatly facilitates calibration.

Beside the conventional optical trap which is based on a single microscope objective, novel optical trapping approaches or concepts have also been developed, including holograms [34] and surface plasmon (SP) based nano lenses [35]. Holograms have been used to generate complex and high-order optical trapping beams by placing a diffractive element in a plane optically conjugate to the back aperture of the microscope objective. Zhijun Sun et al. [35] showed that light can also be focused by a special setup of nanostructures instead of the conventional lenses. They found that the transmittance and phase of light through a subwavelength nanoslit array can be controlled with proper design of the slit depth/metal thickness. Based on these results, they showed that it was possible to focus or collimate photons using only nanoslits. The method was used to built a convex metal bump with nanoslits, adjust the slit depths thus to control each phase shift. This nano lens gives the advantage in building a compact size optical trapping.

1.1.4 Optical trapping application in biology research

Modern position detection systems are able to measure the position of a micro-sized sphere with an accuracy of 10 nm. The trap stiffness depends on the design of the traps and the size of the trapped objects and varies from 1 pN/μm (per mW of laser power) to 50 pN/μm (per mW of laser power). In most biological assays with optical traps, a micron-sized glass or polystyrene bead is trapped biochemically attached to a biological specimen, serving as a "handle" for the optical

tweezers to grab. Displacement of the bead in the focal plane can be tracked with nanometer and millisecond resolution by imaging the sphere onto a quadrant photodiode.

Single or multiple optical traps have been developed to measure the properties of DNA [26], step movements of motor proteins [25, 27] and pushing forces [28] and pulling forces [29] of microtubules.

1.2 HEAT GENERATED BY ELECTROMAGNETIC WAVES SIMULATED METAL NANOPARTICLES

1.2.1 Heat effects of metal nanoparticles in the presence of electromagnetic radiation

If an electromagnetic wave of a given frequency strikes an object with similar resonant frequency of vibration of the electron electrons, then electrons of the material will absorb the energy of the electromagnetic wave and transform it into vibrational motion. During the process, heat generates. Metal NPs have strong light absorbing properties since they have many mobile electrons. They efficiently generate heat if the frequency of electromagnetic wave matches their plasmon resonance. The plasmon resonances in metal NPs can be adjusted by changing sizes, shapes, the composed materials of nanoparticles [12, 13, 18], or organization of nanoparticles assemblies [9]. The local heating effects and the unique size-dependent photo-thermal conversion properties make metal nanoparticles or nanostructures promising tools for a wide range of applications in biology research, life science, biomedicine and physics.

1.2.2 Heating mechanism

The heat generation process involves photon absorption and heat dissipates from NPs to surrounding matrix. The mechanism of heat release can be explained as the laser electric field strongly drives mobile carriers inside the nanoparticles, and the vibrational energy gained by carriers convert into thermal energy in terms of heat. Then the heat diffuses away from the nanoparticles and increases the temperature of the surrounding material.

The total amount of heat generated from a NP can be simply estimated from Joule heating. In the presence of applied electromagnetic field $\vec{E}_0$, the local heat intensity $Q(\vec{r},t)$ (rate of heat generation per unit volume) comes from light dissipation in the metal NP [30, 19, 36, 37, 38]:

$$Q(\vec{r},t) = < \vec{j}(\vec{r},t) \cdot \vec{E}(\vec{r},t) >_t = \frac{\omega}{8\pi} | E(\vec{r}) |^2 \ \mathrm{Im}\, \varepsilon_{NP} . \tag{30}$$

where $\vec{j}(\vec{r},t)$ is the current density as a function of $\vec{r}$ and time t, $\vec{E}(\vec{r},t)$ is the local electric field and ε_{NP} is the dielectric function of nanoparticles. To calculate $Q(\vec{r},t)$, we assume the size of a metal NP is much smaller than the incident light wavelength, so that electrons inside the nanoparticles experience the same homogeneous electromagnetic field and respond collectively. The local electric field $\vec{E}(\vec{r},t)$ inside a spherical body can be expressed as:

$$\vec{E}(\vec{r}) = \frac{3\varepsilon_0}{2\varepsilon_0 + \varepsilon_{NP}} \vec{E}_0(\vec{r}) . \tag{31}$$

where $\vec{r}$ is the coordinate, ε_0 is the dielectric function of the surrounding matrix. Then heat generation rate can be described as:

$$Q = \frac{\omega}{8\pi} E_0^2 \, | \frac{3\varepsilon_0}{2\varepsilon_0 + \varepsilon_{NP}} |^2 \, \mathrm{Im}\, \varepsilon_{NP} \,. \tag{32}$$

In the absence of phase transformations, the temperature of a system consisting of a homogeneous NP can be found solving the heat transfer equation:

$$\rho(\vec{r}) c(\vec{r}) \frac{\partial T(\vec{r},t)}{\partial t} = \nabla k(\vec{r}) \nabla T(\vec{r},t) + Q(\vec{r},t) \,. \tag{33}$$

where $T(\vec{r},t)$ is local temperature, $\rho(\vec{r})$, $c(\vec{r})$ and $k(\vec{r})$ are the mass density, specific heat, and thermal conductivity, respectively. For a single spherical NP, the involved solutions of this system are given analytically by Goldenberg and Tranter [39]. In the steady-state regime, the local temperature around a single NP is given by:

$$\Delta T(\vec{r}) = \frac{V_{NP} Q}{4\pi k_0 r} . \qquad (r > R_{NP}) \tag{34}$$

where r is the distance from the center of an NP, k_0 is the thermal conductivity of the surrounding medium, V_{NP} and R_{NP} are the NP volume and radius, respectively. The maximum temperature increase occurs at $r = R_{NP}$ and is described by:

$$\Delta T_{\max}(I_0) = \frac{R_{NP}^2}{3k_0}\frac{8\pi \cdot I_0}{c\sqrt{\varepsilon_0}}\frac{\omega}{8\pi}\left|\frac{3\varepsilon_0}{2\varepsilon_0 + \varepsilon_{NP}}\right|^2 \operatorname{Im}\varepsilon_{NP}. \quad (35)$$

where I_0 is the light intensity inside the matrix.

We see from Eq (35) that the temperature increase is size dependent and it is proportional to the second power of R_{NP}. Phase transformation in a surrounding matrix becomes possible if a nanoparticle size is large enough. The heat generation rate and temperature increase also depend on the imaginary part of the dielectric constant of a NP, which reflects the absorption property. For a metal NP at surface plasmon resonance, at where electrons experience the same homogeneous electromagnetic field and respond collectively, it shows strong absorption of light around the resonance wavelength. The total heat generation rate $q_{tot} = V_{NP}Q$ usually demonstrates a typical plasmon peak. In gold and copper nanoparticles the surface plasmon resonance is located in the visible (e.g., ~530 nm for gold NPs) [12, 13]. In silver, the surface plasmon resonance peaks in the near UV [12, 13].

Because the heating effect becomes strongly enhanced at plasmon resonance, the applications of metal nanoparticles are usually operated at their plasmon resonance wavelengths. Long-wavelength operation is desirable in biomedical applications of heated NPs because long wavelength reduce absorption by the biological medium (e.g., alleviates radiation damage), and also provide good penetration depth. Shifting of plasmon resonances by changing the sizes, shapes or composed materials of NPs have been intensively studied. Au nanorods and nanoshells have plasmon resonances shifted to the red (650-900 nm) [8, 40]. Single-walled carbon nanotubes have been reported showing heating enhancement at radiofrequency (RF) range [41].

Heating efficiency can be strongly enhanced in the presence of several NPs. NPs form small complexes of different geometry and each complex can have a unique thermal response [9]. This may due to an increase of a volume of metal and electric-field amplification, and theoretical work describing the collective thermo-optical responses of metal NPs assemblies has also been reported [9, 42].

1.2.3 Biomedical applications

This photo-thermal conversion effect in metal NPs has been extensively investigated for thermal-related medical imaging, tumor destruction via heating and remote release of drugs. The related imaging techniques by heated NPs include photothermal, photoacoustic and thermoacoustic imaging. In photothermal imaging, heating generates by applied electromagnetic energy subsequently modifies itself the optical properties, which can be recorded optically. The heating also causes subsequent thermal expansion, which produces an acoustic wave that is measured by an array of photoacoustic and thermoacoustic sensors [43, 44].

Tumor destruction via heated NPs relies on a simple mechanism [8, 10]. In this case, NPs are first appropriately functionalized and then bind specifically to certain tumor. Then electromagnetic wave stimulated NPs will be heated locally, rising the surrounding temperature to destruct the malignant cells. Generating heat in a local confined space by metal NP colloidal solutions for RF ablation of cancer has been reported [21, 22, 23, 24]. The application on remote release of drugs involves phase transformations of the surrounding material under heating. A polymer is coated on Au NPs which may also contain drug materials. The polymer capsule is destroyed as a result of the heating effect [20].

2.0 OPTICAL TRAPPING BY METALIC NANOSLIT LENSES

As microfluidic devices become a platform technology for small-analyte-amount analysis in lab-on-a-chip configuration for biomedical applications, miniaturized optical lenses have been drawing increasing attention for use in optical trapping on a chip. Embedding an optical trapping function into a lab-on-chip system will enable the development of ultra compact multifunctional systems [45]. Dielectric lenses, which are commonly used in conventional optical trappings, shape an incident light info a sharp focus by refracting the beam at curved surfaces of the lenses with index contrast. However, the transmitted beam shows a strong diffraction effect at lens edges. This causes the focusing capability deteriorating when conventional optics components are scaled down to a wavelength or subwavelength range.

Recently, metal nanoslit array structures were proposed as an alternative to conventional refractive lensing [35]. The beam can be shaped by adjusting structural and/or materials parameters of nanoslits. All these features offer great flexibility in designing compact chip-scale lenses. In this chapter, we theoretically analyze the beam profiles shaped by metal nanoslit arrays and optimize the design for trapping micron-size beads by a 1064 nm laser. We fabricated planar metallic nanoslit lenses using a combination of electron-beam lithography and thin film thermal evaporation. We demonstrate experimentally trapping polystyrene microspheres in a fluidic channel by using these metallic nanoslit lenses. This is the first experimental demonstration

(realization and utilization) of novel metallic lenses that offer unique advantages of integration and flexibility over conventional dielectric lenses.

2.1 THEORETICAL ANALYSIS

Beam shaping by a surface plasmon-based metallic nano-optic lens has been reported by Zhijun Sun and Hong Koo.Kim in 2004 [35]. The lens is a convex-shape, composed of a metallic nanoslit array with tapered metal thickness. A plane wave is incident upon the lens bottom and excites a surface plasmon (SP) mode at the slit entrance. For a single slit, the SP wave propagates along the slit region with a complex propagation constant, and then decouples into radiation modes at the slit exit, diffracting into all radial directions with a uniform power distribution. The amplitude (i.e., transmittance) and the phase of the output beam are complex functions of the structural and materials parameters (such as slit width, depth and spacing, and dielectric constants) and the operating wavelength relative to slit spacing. When these parameters are carefully chosen, it is possible to focus light above the metallic arrays.

Here we use the superposition method to simulate beam shaping by a planar metallic nanoslit array. The dispersion relation of an infinite single metal slit with width *w* is given by [35]:

$$\frac{\sqrt{N_{eff}^2-\varepsilon_D}}{\varepsilon_D}\tanh\left(\sqrt{N_{eff}^2-\varepsilon_D}\,\frac{k_0 w}{2}\right)+\frac{\sqrt{N_{eff}^2-\varepsilon_M}}{\varepsilon_M}=0\,. \qquad (36)$$

where ε_D and ε_M are the dielectric constants of the material fulfilled the slit and metal, respectively, k_0 is the vacuum wave vector and N_{eff} is the effective refractive index and is defined as:

$$N_{eff} = \frac{k_{sp}}{k_0} = \frac{k'_{sp} + ik''_{sp}}{k_0}. \tag{37}$$

N_{eff} can be solved from Eq.(36), and then for a single slit with *d* length, the phase of the wave at the slit exit can be calculated by the below formula:

$$\phi = \mathrm{Re}(N_{eff})k_0 d. \tag{38}$$

For a slit array with multiple nanoslits of the same length but different width, the radiation wave coupled from SP wave that exits from each nanoslit element is resembled as a cylindrical wave with the initial phase ϕ. The intensity at any spatial point can be calculated by the superposition of all of these waves.

Figure 3 (a) shows a three-slit metallic lens structure in water ambient that is simulated by the superposition method. The three slit widths are all 40 nm and the slit center to center spacing (dg) is 460 nm. The metal is gold and the thickness is 120 nm (Fig. 3 (a)). A TM-polarized plane light with a 1064 nm wavelength is incident from air to the bottom side. The dielectric constant ε_m = -53.99-i4.19 is used for gold [46]. As shown in Fig. 3 (b), the transmitted wave becomes sharply focused above the slit array. The axial intensity profile (x = 0) and the transverse intensity profile (y = 0.65 μm) of the main beam are plotted respectively in

Fig. 3(c) and Fig. 3 (d). The focus occurs at 0.65 μm above the slits with a transverse beam width of 520 nm. Two side beams also propagate in other direction, however, they can be neglected since their intensities are less than 15 % of the main beam.

Figure 3 (c) and (d) also indicate that axial confinement is weaker than the transverse confinement for the 3-slit array structure. To improve the axial confinement, we investigate the effects of the slit width of each slit element, slit spacing and the number of slits on beam shaping. The axial intensity distribution for a three-slit array with the same slit spacing but different slit width sequence (60nm, 40nm and 60 nm) is plotted in Fig. 4 (a). Compared with the array with the same slit width, the width-taped array lens shows slightly enhanced confinement round the focal point. The effect of changing slit spacing is shown in Fig.4 (b). It seems that tuning the slit spacing can change the beam profile more dramatically. Increased slit spacing leads to increase of the distance between the focus, however, the gradient degrades and the intensity drops as well.

The radiation force of an optical trap is a function of both electric field gradient and intensity; therefore, to achieve a good trapping performance, an ideal 2D metallic lens should be able to provide a strong intensity gradient for both the transverse and axial directions. It is also desirable to have high transmittance at the optical trapping wavelength. The SP resonance condition of a metal nanoslit is given by [47]:

$$\lambda = \frac{L}{m}\sqrt{\frac{\varepsilon_d \varepsilon_m}{\varepsilon_d + \varepsilon_m}}\,. \tag{39}$$

where L is the slit spacing, m is the order of the grating vector involved in SP coupling, and complex ε_m and ε_d are the dielectric constants of metal and adjacent dielectric, respectively. According to this formula, a gold nanoslit array on quartz in water ambient requires its slit

spacing to be about 750 nm to get a transmittance peak at 1064 nm. However, this slit spacing is apparently too large to have a good axial confinement. A compromise is to use a multiple-slit array with small slit spacing. We investigate 3-slit, 5-slit and 7-slit arrays with the same slit element width which are easier to fabricate. By tuning the slit spacing and considering the gradient as the most important factor, a 3-slit array with 460 nm slit spacing and 40 nm element slit width, a 5-slit array with 300 nm slit spacing and 40 nm element slit width, and a 7-slit array with 250 nm slit spacing and 40 nm element slit width are chosen and the axial intensity distribution are plotted in Fig. 4 (c). Among these three arrays, the 7-slit array shows higher gradient, intensity and longer focus length (1.2 μm), and should have a better trapping performance.

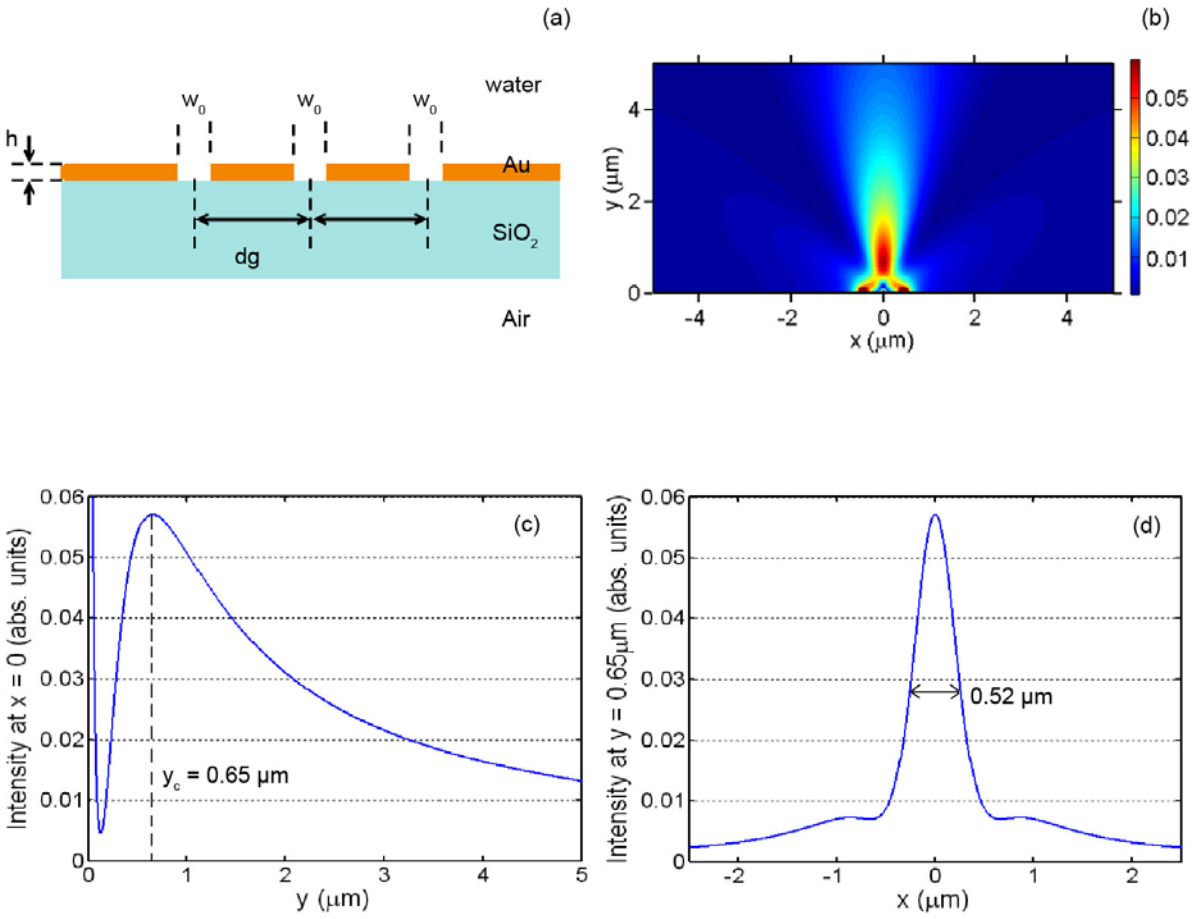

Figure 3. A planar metallic lens based on a nanoslit array. (a) Geometry of the lens consisting of a 120 nm-thick gold film (orange) with three slits of 40 nm widths and 460 nm slit center to center spacing (dg). (b) Focusing pattern of the field intensity through the center of the slits by the superposition method. (c) Axial beam intensity profile along the propagation direction (x = 0). The focus length is 0.65 μm (y_c = 0.65 μm). (d) Transverse beam intensity distribution at the focus (y = 0.65 μm). It shows that the beam width is about 0.52 μm.

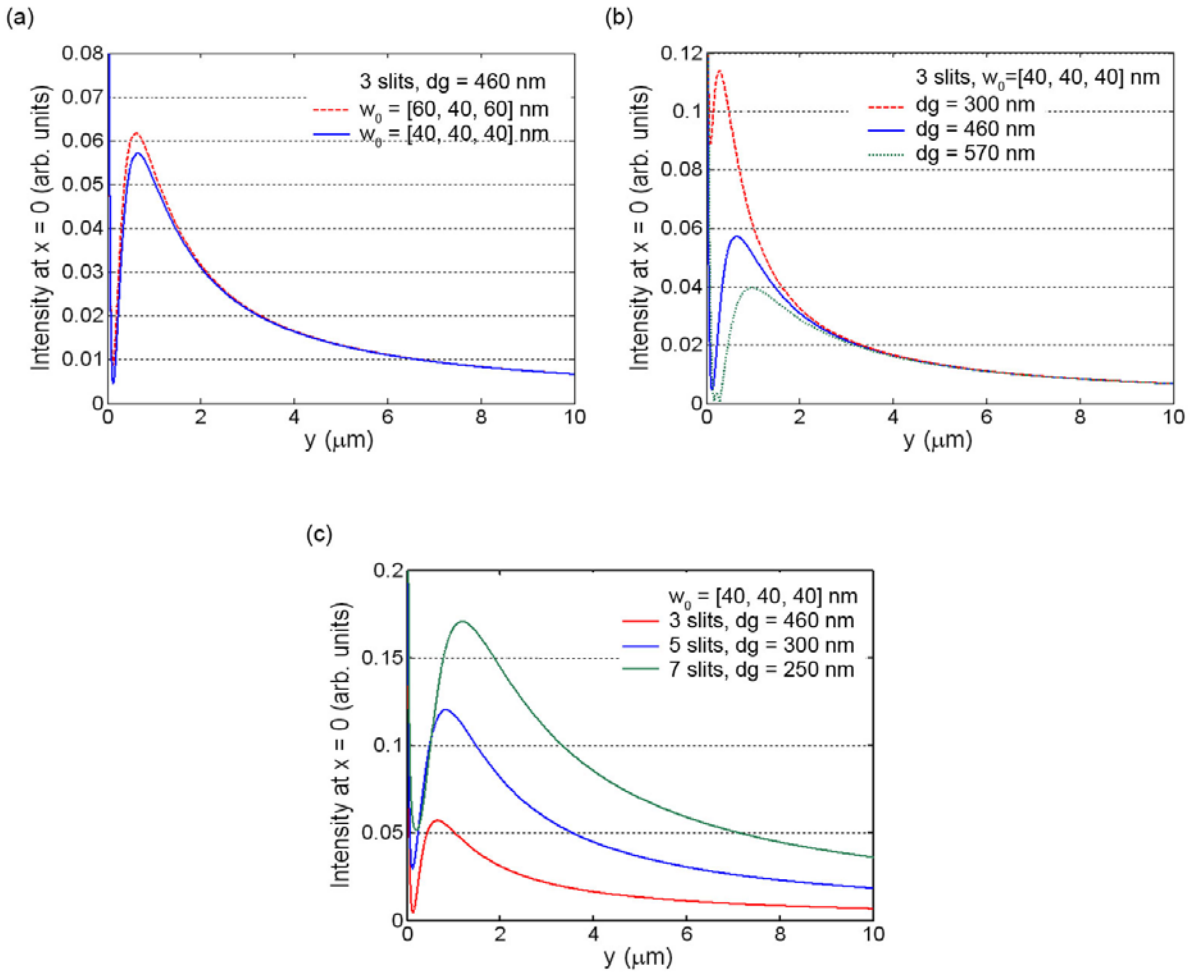

Figure 4. Intensity distribution along the axial direction for nanoslit arrays. (a) 3-slit arrays with same slit spacing but different slit width sequence (set of 60 nm, 40 nm and 60 nm versus set of 40 nm for all three slits); (b) 3-slit arrays with same element slit width but different slit spacing; (c) 3-slit array with 460 nm slit spacing and 40 nm element slit width, 5-slit array with 300 nm slit spacing and 40 nm element slit width, and 7-slit array with 250 nm slit spacing and 40 nm element slit width.

2.2 FABRICATION AND EXPERIMENTS

The nanoslit array lenses are fabricated using electron-beam lithography, plasma etching technique and the angle deposition of metal method. Three 50-μm long nanoslit array patterns with 130 nm element slit widths are made, which are a 3-slit array with 460 nm slit spacing, a 5-slit array with 300 nm slit spacing, and a 7-slit array with 250 nm slit spacing. The etch depth into the quartz is 200 nm for each 130 nm wide slit. These quartz mesas serve as modes and a 6 nm-thick Cr thin film is first evaporated on it, followed by a 127 nm-thick gold layer. Cr thin film is used to improve the adhesion of gold on quartz. For the metal film, we opt for gold because it does not oxidize in water and also it has a good plasmonic response for visible light. The deposition angles of two metals are 30^o with respect to the normal to the substrate. Depositing metal at a tilted angle is to prevent metal from covering the entire surface of a mesa structure. We choose 30^o as the deposition angle so that the final gap between gold islands would be around 40 nm.

A flow cell consisting of a cover glass, and polydimethylsiloxane (PDMS) (Sylgard 184, Dow Corning) thin films and PDMS base with channel patterns of the same depth and inlet and out let tubing is assembled to encage the nanoslit sample. The nanoslit substrate is first seating on a rectangular channel on the PDMS base. The depth of the channel is slightly greater (~70 μm) than the thickness of the substrate. A piece of cover glass which size is larger than the rectangular channel is used to cover the groove. A large and thin PDMS film is then placed on to cover all the area and seal the channels because of good adhesions of the thin PDMS film to glass and PDMS base. Right on the cover glass, a window is cut on the PDMS thin film. Without doing that, the microscope objective cannot get close enough to focus on the nanoslit. Figure 5 shows the assembled flow cell.

In optical trapping experiment, two 1 mL syringes are connected to the inlet and outlet tubing separately. 0.05 wt% polystyrene beads of 2 μm diameter (Alfa Aesar) suspended in 0.5 mg/mL bovine serum albumin (BSA) aqueous solution are fulfilled into the PDMS channel by pulling one of the 1 mL syringe. BSA serves as a carrier in solution to prevent permanently sticking of polystyrene beads on the gold surface. The flow speed is controlled by adjusting the height difference between the liquid surface in inlet tubing and in outlet tubing.

The entire flow cell is then placed on an upright microscope stage. A 100× oil immersion microscope objective is used to observe the motion of beads abound the nanoslit arrays. Movies of the PS bead movements are taken by a Nikon Coolpix 995 digital CCD camera in 15 fps. A tungsten lamp is used for white light illumination.

The optical configuration of the experiment is illustrated in Fig. 6. A diode pumped solid-state laser (λ = 1064 nm) is used as the laser source. While a collimated input laser beam is sufficient to form a trap, a 10× DIN objective (0.25 NA) is used to enhance the intensity of laser beam because the effective incident power of the laser after the optics is limited at 32 mW. The laser spot illuminating at the metal/water interface has a 50 μm diameter. The corresponding intensity is calculated to be 2×10^7 $W \cdot m^{-2}$. This intensity is more than one order of magnitude weaker than the intensity of a conventional optical trapping ($\sim 10^9$ $W \cdot m^{-2}$). Although the incident laser beam is not collimated, trapping beads by the low NA objective is difficult and thus the trapping effect due to the 10× objective is neglected.

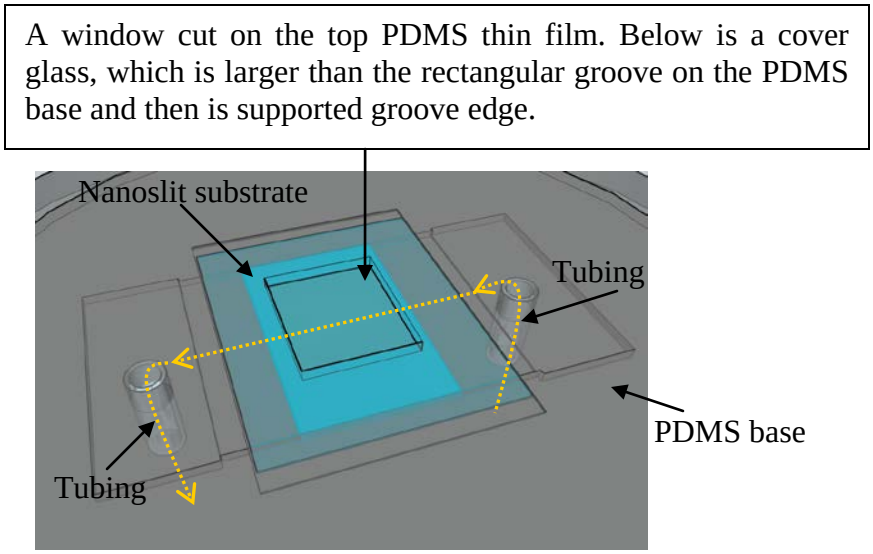

Figure 5. Schemes of the structure of flow cell used to test the metallic nanoslit lenses for optical trapping. The yellow stream line indicates the fluid flow direction.

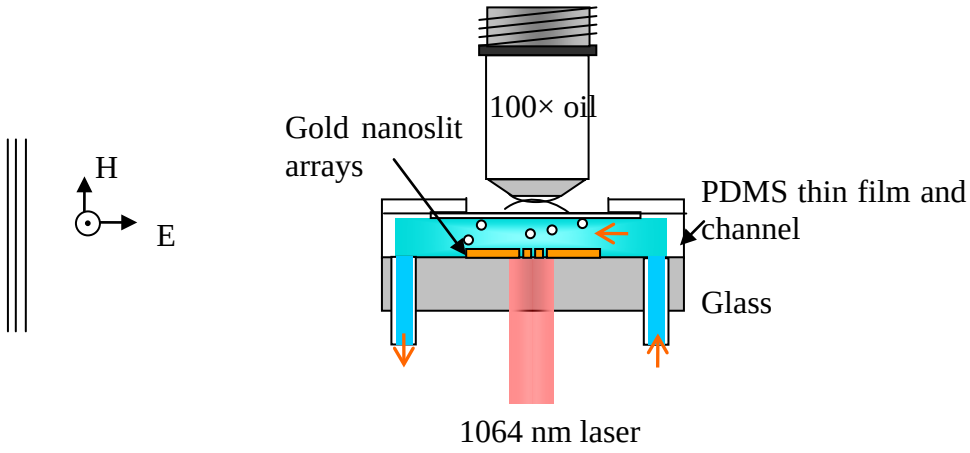

Figure 6. Experimental setup for the optical trapping by metallic nanoslit lenses in a flow cell. The left side figure shows the TM-polarization of the incident wave to the nanoslit.

2.3 RESULTS AND DISCUSSION

The 7-slit planar nanoslit trap is tested first. The trap is formed when the trapping laser illuminates normally from the bottom side. When no fluid flow is applied, polystyrene beads drift in the channel by thermal motion. Because the focal region is relatively close to the substrate surface, only those that diffuse near to the arrays and are close to the floor can be captured by the traps. Once a bead is trapped, it remains there and can move only along the slit direction. Figure 7 (a) shows several polystyrene beads trapped by the 7-nanoslit lens. In this photograph, both beads and nanoslit array are clearly visible because the trap focus is only 1.2 μm above the substrate. When a fluid flow is applied, beads are forced away from the trap, which indicates the trapping force is relatively weak. When the polarization of the incident laser is switched from TM mode to TE mode, beads are released and cannot be trapped any longer. This observation is consistent with the theory that SP wave only can be excited by TM-polarized incident wave. When the incident laser is turned off, beads are released and diffuse into the water. The 5-slit lens and 3-slit lens also can perform trapping and show similar behavior.

To estimate the trapping force, a hydrodynamic drag-force approach is used to measure the escape force. Figure 7 (b) shows the fluid flow direction with respect to the nanoslit array. First the applied flow rate is set low enough so that the bead remains trapped when it approaches the edge. The fluid flow is then gradually increased until the bead escaped from the traps at zero velocity. The movement of beads during changing the flow rate is recorded as movies. Tracks of beads are traced and analyzed by a Matlab program. The velocities of beads are calculated by fitting the position and time curve and the slope gave the average velocity during the time frame. The critical flow velocity is assumed to be the incident velocity of the bead at the point when the escape velocity becomes near zero.

Figure 7 (c) shows the traces of several 2 μm diameter polystyrene beads at the same focal plane when they are passing through the nanoslit with different velocity. The green trace indicates a process that the bead is entering the trap, getting captured for less than one second and then escaping the traps at a near-zero velocity. The entering velocity is calculated to be 1.9 μm/s (from the red slope) and is considered as the critical velocity. The purple and magenta traces indicate that these beads enter into the traps at a velocity higher than critical velocity, and thus cannot be captured. To calculate the escape force by the modified Stokes's formula, $1x10^{-3}$ Pa·s is used as the viscosity of 0.5mg/mL BSA, and the distance between the bead and the floor is assumed to be 100 nm. The results show that escape forces for the 7-nanoslit, 5-nanoslit and 3-nanoslit array lenses are 0.071 pN, 0.062 pN and 0.060 pN. The force is relatively weak and the differences are within the error bars of measurement. However, it may show a trend that a nanoslit lens with more slits could form a stronger trap. To achieve a greater trapping force, using higher power could be a solution.

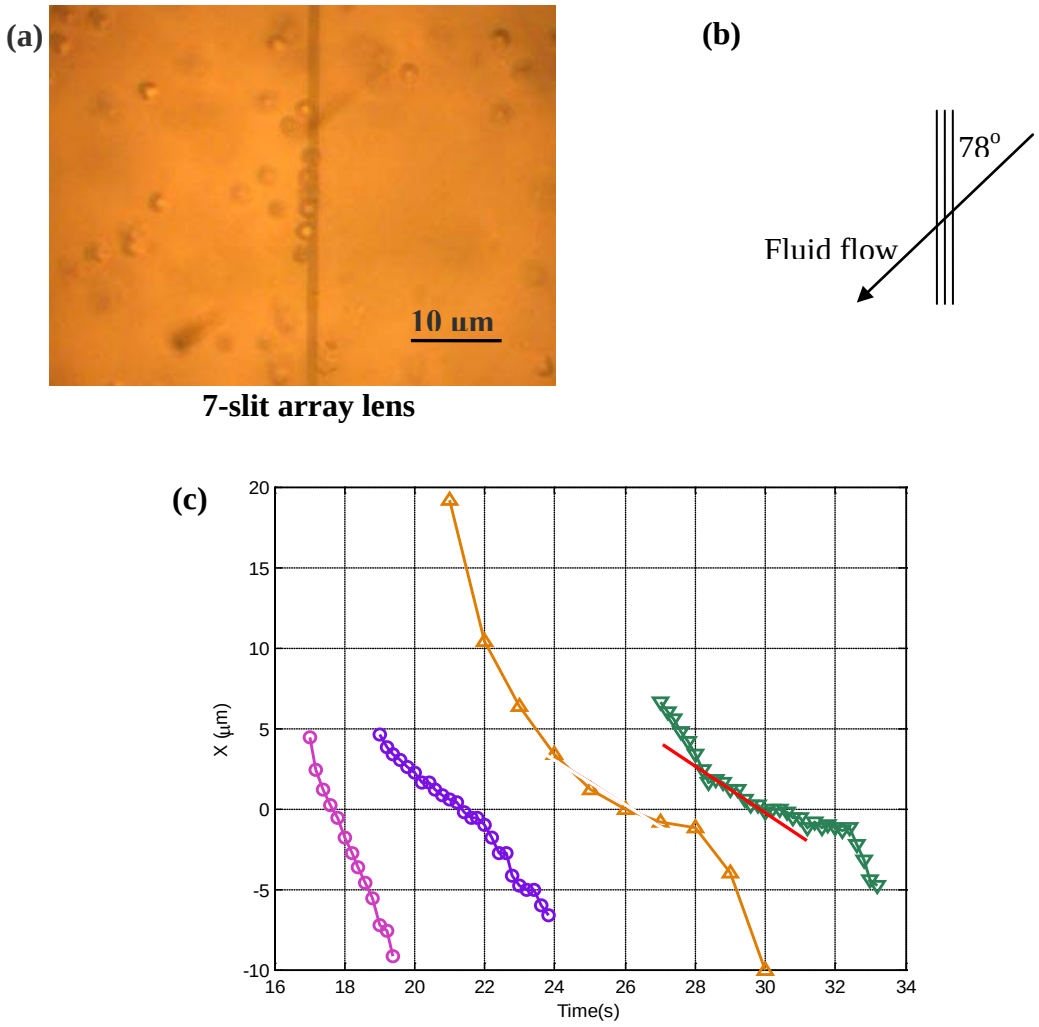

Figure 7. Trapping of polystyrene beads by the 7-nanoslit array lens and measuring the escape force. (a) Several beads are trapped in a line above the nanolist array. (b) Fluid flow direction respect to the slit array when measuring the escape force. (c) Traces of 2 μm diameter polystyrene beads at the same focus plane passing through the nanoslit with different velocities. The entering velocity can be extracted from the green trace which shows that the bead is captured with the incident velocity and escapes at a near zero velocity. The critical velocity is calculated to be 1.9 μm/s (from the red slope).

2.4 SUMMARY

As the biological experiment systems scale down, the conventional optical traps become of limited use due to their bulky sizes. We designed and experimentally demonstrated that metallic nanoslit arrays can focus light and work as optical traps. By changing the slit width, slit spacing and number of slit, the trapping performance can be changed. The escape forces of the nanoslit array lenses are in the order of the 0.07 pN with 32 mW incident laser power. The nano-optic traps developed in this study are promising because they can be easily embedded into chip-scale systems and new functionalities can be introduced.

3.0 ON-CHIP OPTICAL TRAPPING BY METAL EDGES AND ITS APPLICATIONS IN BIOLOGICAL PROCESS STUDY AND PARTICLE SORTING

A tightly focused laser beam can trap micron-size objects near its focus if the object has higher refractive index compared to surrounding medium. Trapping force originates from the momentum change as incident light refracts and/or reflects by the object. Since Ashkin's report of this subject phenomenon in 1986 [48], optical trapping has been widely studied and further developed. The advantage of optical trapping is that it can immobilize, manipulate or transport micro objects in a non-contact fashion in microscopic environment. Optical tweezers based on far-field optical trapping has been well-established and become an important tool in biological and physical research. Conventional optical tweezers are a three-dimensional (3D) optical trap formed by focusing a high-power laser beam through a microscope objective with a set of external optics, usually involving a high numerical aperture (N.A.) objective, precise beam expansion and collimation. Optical tweezers have been used to measure the forces generated during biological processes [49] and linear optical translation [50, 51, 52, 53]. An array of multiple optical traps [54] has also been developed for particle sorting and manipulation. While conventional optical tweezers are continuously finding applications, recently there is growing interest in in novel on-chip optical trapping. This trend is due to the fact that microfluidic systems are becoming a common platform for small analyte amount assays and particle manipulation. Almost biological studies are performed in an aqueous environment. When

combined with a microfluidic system, conventional optical tweezers would make the entire system bulky, whereas chip-scale optical trappings are more amenable for compact configuration. Chip-scale optical tweezers can be fully embedded into a microfluidic system, allowing multiple functionalities such as particle sorting, manipulation and biophysical force measurements thus opening the possibility to develop new lab-on-a-chip devices. Several on-chip optical trappings have been demonstrated, e.g., incorporating optical fibers into microfluidic systems [55], Fresnel zone plates [56] and optical tweezers based on plasmonic structures [57, 58, 59]. Although optical fibers are compatible with planar integration, they require precise alignment. Fresnel zone plates have potential to be integrated but the size of plates is relatively large (100 μm) and achieving a compact configuration is not easy. In contrast, optical trapping based on plasmonic structures is considered most promising for chip-scale integration, owing to their flexibility in creating multiple planar traps by a single laser beam. Trapping of micrometer sized dielectric particles has been demonstrated by use of surface plasmons excited around a planar metal disc. More recently, scannable plasmonic trapping using a gold stripe has been reported. In these strategies, surface plasmon polaritons (SPPs) are excited by using a prism as the coupling medium to match the photon and surface plasmon wave vectors. The incident angle needs to be in a specific range and the beam also needs to be polarized. Overall the external optics is complicated.

In this study, we present a novel and easy-to-implement method of two-dimensional (2D) optical trapping. This new method utilizes diffractive transmission of light at an engineered thin-film gold edge structure. We show that a gold thin-film edge formed on a planar chromium thin-film can produce a localized intensity distribution of light around the gold film edge. We demonstrate that this thin film edge can trap polystyrene (PS) microspheres. This optical trapping

can operate with an uncollimated laser beam at relatively low illumination power. No specific beam polarization is required. Moreover, this structure can be flexibly integrated into microfluidic systems. Biological and microfluidic applications of Au/Cr edge trapping are presented. First, dual/multiple trapping of microparticles by patterned metal edges is demonstrated. Use of this dual-trap system for microtubule dynamic study is also discussed. Then, separation and sorting of different-size polystyrene microspheres by an Au/Cr strip is demonstrated.

3.1 THEORETICAL CALCULATION OF OPTICAL TRAPPING FORCE

The structure consists of a gold stripe sitting on a thin planar chromium film deposited on a transparent glass slide as shown in Fig. 8(a). The film thicknesses are 10 nm for Cr layer and 100 nm for gold stripe. The intensity distribution of light at the Au/Cr edge in water ambient is calculated by two-dimensional (2D) finite-difference time-domain (FDTD) method as shown in Fig. 8(b). In the calculation, the incident light is a TM-polarized laser beam of 1064 nm wavelength normally incident to the film. A quasi-parabolic fringe pattern is observed around the edge, which can be explained with reference to the well-known Fresnel diffraction pattern. The first fringe on the left-hand-side of the gold edge has the maximum intensity and decays along the y-direction. This localized intensity distribution is the key aspect that is explored in this thesis for possible optical trapping.

In order to develop a quantitative understanding of underlying physics of possible optical trapping mechanism by a metal edge, a theoretical calculation is performed. Here we present a method to predict radiation force exerted to a dielectrical microsphere by using the ray optics

model in conjunction with the FDTD simulated electric field distribution. In ray optics regime, the dialectic microsphere is considered to be much larger than the wavelength so that diffraction effects can be ignored. Under this approximation, incident beam of light is treated as bundles of individual rays, and each ray has appropriate intensity, direction, and polarization. Each incident ray is scattered by the microsphere, and its reflection and refraction follow the Fresnel formulas.

The total force exerted on the microsphere is contributed by all rays incident into and scattered out of the microsphere. Based on the Fresnel formulas, for a single beam incident with angle θ, the resulting force can be divided into two components, scattering force and gradient force, which are parallel and perpendicular to the incident ray, respectively. These forces are given by Ashkin in 1992 [2]:

$$F_{scat} = \left\{1 + R\cos 2\theta - \frac{T^2[\cos(2\theta - 2\alpha) + R\cos 2\theta]}{1 + R^2 + 2R\cos 2\alpha}\right\}\frac{n_m P}{c}. \tag{40}$$

$$F_{grad} = \left\{R\sin 2\theta - \frac{T^2[\sin(2\theta - 2\alpha) + R\sin 2\theta]}{1 + R^2 + 2R\cos 2\alpha}\right\}\frac{n_m P}{c}. \tag{41}$$

where α is the refractive angle, T and R are the Fresnel transmission and reflection coefficients, respectively, n_m is the refractive index of surrounding medium, P is the beam power and c is the velocity of light in vacuum. These two formulas have taken into account the multiple reflections and refractions inside the microsphere.

In our method, the optical fields and energy flow distribution around the corner are first obtained by performing 2-D FDTD simulation. A three-dimensional (3-D) optical field is constructed by repeating the 2-D optical fields along the z-direction. Figure 8(d) shows the map of Poynting flux around the edge. When a microsphere is placed in it, the electric field of each

FDTD grid with known direction and amplitude on the microsphere surface is treated as an individual ray. The polarization states of each ray should be considered. The portion of s-polarization and p-polarization are given as [60]:

$$f^{s} = \cos^{2}\gamma . \tag{42}$$

$$f^{p} = \sin^{2}\gamma . \tag{43}$$

where γ is the angle between the electric field vector and the incident plane. The contribution of each polarization states to the net force are obtained by the following equations:

$$F_{scat} = f^{s}F_{scat}^{s} + f^{p}F_{scat}^{p} . \tag{44}$$

$$F_{grad} = f^{s}F_{grad}^{s} + f^{p}F_{grad}^{p} . \tag{45}$$

The lateral (radial) and vertical (axial) forces can be calculated by summing over the projection of the net scattering force and net gradient force of each ray to the x- and y-directions. Here we assume the multiple reflections between the microsphere surface and the substrate is insignificant. The reason is that the divergence of Poynting flux is small in this work and flux is mostly upward. The reflection coefficient for 45^{o} incident angle (in this condition multiple reflections between the microsphere surface and the substrate may happen) is 2.4×10^{-2} for *s* polarization and 5.6×10^{-4} for *p* polarization (refractive index of water and PS microsphere is 1.33 and 1.60, respectively, at 1064 nm). Thus we consider multiple reflections between the microsphere surface and the metal substrate can be ignored.

The gravity and the buoyancy affect the vertical component of forces exerting on the sphere, so that they should be included in the calculation. Figure 9 shows the contour map of the radiation force components exerted on a 2-μm-diameter PS microsphere (density, 1.06 g/cm^3). Each point on the map corresponds to the center position of the microsphere. A microsphere can stay at those locations where both lateral and vertical forces are zero. The balanced location nearest to the edge is found to be at $x \approx -1.3$ μm. At this x-location, the microsphere experiences zero vertical force. Any displacement along the positive x-direction will cause downward and leftward restoring forces. Displacement along the negative direction will cause a rightward restoring. To escape the trap from the left-hand side, the escaping force of 0.05 N is estimated to be required. In this trapping strategy, stable trapping significantly depends on the transmitted beam power on the non-gold-covered area. Use of a semitransparent thin-film Cr layer is important in that it offers a degree of freedom in adjusting the transmitted power to the level proper for vertical confinement of power therefore for vertical trapping.

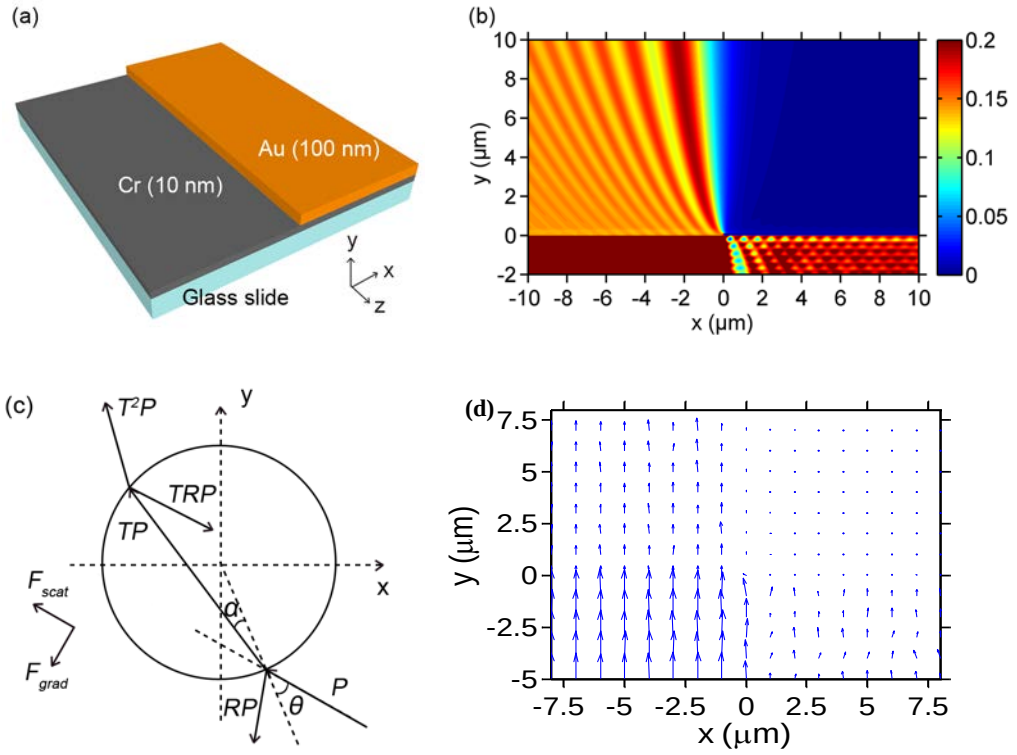

Figure 8. Calculation of the optical force around an Au/Cr edge trapping. (a) Schematic of a Au/Cr edge trapping structure that comprises a gold stripe sitting on a planar Cr thin film on a glass slide in water ambient. (b) 2D FDTD calculated intensity distribution of light around the Au/Cr edge. (c) Ray optics model for calculation of radiation force exerted on a dielectric microsphere. (d) Distribution of Poynting flux.

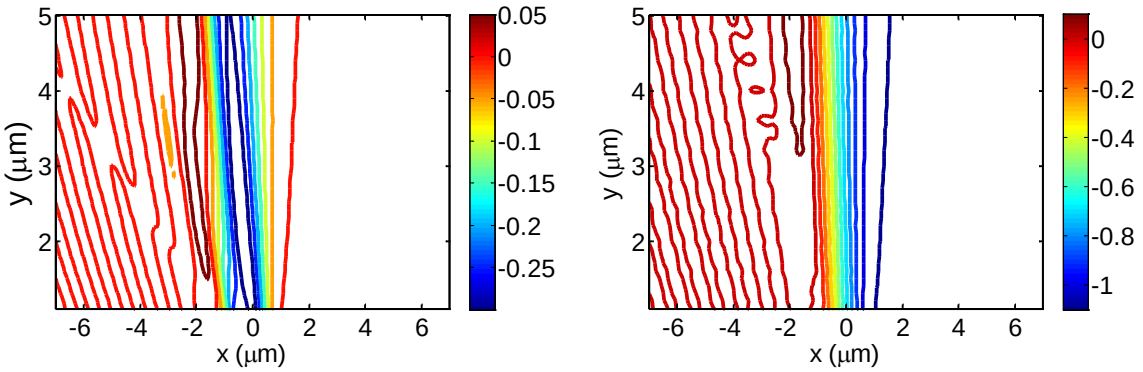

(a) (b)

Figure 9. Contour map of the radiation force components exerted on a 2-μm-diameter PS microsphere. (a) lateral force. (b) vertical force.

3.2 FABRICATION AND FORCE CHARACTERIZATION

The gold edge structure is fabricated on a glass slide by photolithography and thermal evaporation, followed by a lift-off process. A planar Cr layer of 10-nm thickness is first thermally evaporated on a clean glass slide. Photoresist (SC1805: S1027 = 1:1) of 1.2-μm thickness is then spin-coated on the Cr surface. By using the photolithography technique, 60-μm–wide photoresist stripes are formed on the Cr surface. Gold is then thermally evaporated on the photoresist patterned substrate. The thickness of gold is about 110 nm. After a lift-off process in acetone, the structure of Au stripes on a planar Cr is formed. As illustrated in Fig. 10(a), the Au/Cr stripes on substrate is caged in a microfluidic channel (of 75-μm height and 2-mm width) having both an inlet and an outlet. The microfluidic channel structure is fabricated in polydimethylsiloxane (PDMS) (Sylgard 184, Dow Corning) using the standard soft lithography technique. Polystyrene latex microspheres of varying diameters (Alfa Aesar) that are suspended in 0.5 mg/mL bovine serum albumin (BSA) aqueous solution are injected into the PDMS channel by pulling a 1-mL syringe connected to the outlet through a Tygon tubing. In this experiment, the BSA solution is designed to enhance transport of microspheres through the microfluidic channel. Without use of BSA, PS microspheres are prone to get attached on the Cr and Au surface. The flow rate is controlled by adjusting the pulling speed of the syringe. The angle between the flow direction and the gold edge (θ) is designed to be 90 degree (Fig. 10 (b)).

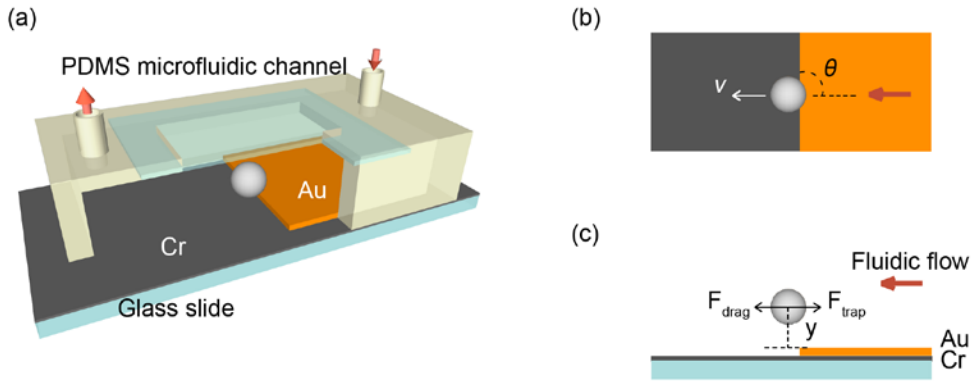

Figure 10. Force measurement for the Au/Cr edge trapping. (a) Optical configuration and the side view of the flow cell. The arrows indicate the flow direction. (b) Top view of the flow cell; the angle between the gold edge is θ; PS microspheres move across the gold edge with an incident lateral velocity v. (c) Schematics of a trapped PS microsphere experiencing forces in a flow cell.

The PDMS cell is placed on an upright microscope stage and a 40× micro objective is used to observe the motion of microspheres around the gold edge. Videos of the PS microsphere movements around the gold edge are taken by a CCD camera (Nikon Coolpix 995) in 15 fps. A tungsten lamp is used for white light illumination. A diode-pumped solid-state laser (λ_0 = 1064 nm, maximum output power = 50 mW, BWR-50E, B&W Tech) is used as the laser source. While a collimated input laser beam is assumed in our model calculation, a 10× DIN objective (N.A. = 0.25, W.D. = 6.3 mm, Edmund) is used to enhance the beam intensity (the maximum incident power available is 32 mW, and this power level is found to be insufficient for trapping. It should be noted that the 10× objective makes the incident beam diverge. To minimize the effect of this divergence of incident beam, we align the focus of the 10× objective such that it forms at the position below the gold surface and the diameter of the laser spot illuminated at the gold/water interface be about 20 μm. We assume the divergence of the incident beam around the gold edge (-5 μm < x < 5 μm) due to the 10× objective is negligible. The corresponding intensity is calculated to be 1×10^{8} $W\cdot m^{-2}$. This intensity is one order of magnitude weaker than the intensity of a conventional optical trap ($\sim10^{9}$ $W\cdot m^{-2}$).

The hydrodynamic drag-force approach is used to measure the escape force. A microsphere is driven by the fluidic flow incident normal to the gold edge. The flow rate is set initially low so that the microsphere can be trapped when it approaches the edge. The total lateral forces experienced by the trapped microsphere in fluidic flow are analyzed in Fig. 10(c). When a microsphere is stably held in the trap, this indicates that the trapping force is equilibrated by the drag force. The hydrodynamic drag force can be calculated from the flow velocity at the center of the microsphere and viscous drag coefficient by using the modified Stokes's theorem [5, 31]. The fluidic flow is then gradually increased, and this results in drag force increase. The

microsphere is forced to get displaced from the center, and this leads to trapping force increase. At a critical fluidic flow rate, the drag force exactly equals the maximum trapping force that the edge trap can provide. Beyond the critical point, the microsphere is no longer trapped and escapes from the trap by thermal motion. We record the movements of microspheres during changing the flow rate. The traces of microspheres are tracked by the Matlab program for microsphere velocity calculation. The critical flow velocity is measured from the velocity of the microsphere immediately after the departure from the trap.

3.3 OPTICAL TRAPPING OF MICROSPHERES BY AN AU/CR EDGE

Trapping PS microspheres of 2-μm diameter is first examined. Microspheres are carried by a fluid flowing perpendicular to the gold edge. A TM-polarized laser beam with 1064-nm wavelength is normally incident to the gold edge from the bottom, and the effective incident power is 32 mW. Figure 11 shows three 2-μm-diameter PS microspheres that are trapped along the edge when they approached the edge from the gold side. By adjusting the focus of microscope, we find the distance between the microspheres and the gold surface is less than 1 μm. In the lateral direction, the microspheres are at $x \approx 0.8$ μm. These results agree with the prediction that the microspheres are trapped at a forward position (on the side without Au). When polarization of the incident laser is switched from TM to TE mode, it is confirmed that microspheres are still trapped. In TE polarization, no surface plasma wave can be excited. Thus we can rule out the enhanced localized near-fields of metallic edge by surface plasma excitation [57, 58]. This trapping method is polarization-independent, and offers advantage over the plasmonic optical trapping in that no specified SP resonance condition needs be satisfied. It

allows external optics can be further simplified. Multiple trapping can be easily achieved by a single incident laser beam.

To measure the escape forces, the fluidic flow is gradually increased until PS microsphere leaves the trap. For a 2-μm-diameter PS microsphere at incident power of 32 mW, the escape velocity is measured to be 49 μm/s. The drag force calculated from the modified Stokes's theorem is 2.2 pN, with the following assumptions: the gap between the bottom of microsphere and the metal surface is 100 nm and the rate fluid flow is same as the speed of the escaping microsphere. The discrepancy between predicted (Fig. 9) and measured escape force may due to the divergence of the incident beam. The divergence of the incident Gaussian beam after the 10× objective is calculated to be 0.16 rad (9 degree) by using the ray transfer matrix method. Although the focus of the 10× objective has been aligned away from the gold surface to minimize the effect of beam divergence, it appears that extra gradient beside the one caused by the diffraction pattern still exists. However, the gradient introduced by the beam divergence should not be significant because no trapping occurs without the gold edge.

The measured escape forces for a 2-μm-diameter PS microsphere at various power levels are plotted in Fig. 12 (a). The result shows that escape force is proportional to incident laser power. According to the ray optical theory for a conventional trap, the gradient force depends on laser power, the size of microsphere and its refractive index. The slope is calculated to be 0.08 pN/mW. This slope value is on the same order as that of a conventional optical trap formed by a microscope 63× objective (0.17 pN/mW [61]). Trapping is observed for PS microspheres with diameter ranging from 0.5 μm to 6 μm. Escape forces for microspheres of different diameter are measured and plotted in Fig. 12 (b). As seen in the figure, the lateral escape force increases with the microsphere diameter. This can be explained by the fact that the trapping force varies as r^3

when the diameter is significantly smaller than the wavelength (in Rayleigh regime), whereas it is independent of the radius when $r >> \lambda$ [2]. At the intermediate regime where $r \approx \lambda$, a linear relationship between the trapping force and microsphere diameter is expected, which has been reported for conventional optical traps [2, 3, 62]. Our results also show the trend that force rising rate slows down when microsphere size increases.

As shown in the theoretical calculation section, the degree of vertical confinement highly depends on the sum of the gravity, buoyancy and upward radiation force. In our experiments, the Cr thin film is critical for vertical confinement. Trapping is only observed at the edge with planar Cr thin film underneath, while no trapping is observed when no Cr layer is used. If the incident power is same for both cases, this could be easily explained as that the transmitted power is too strong and it repels microsphere from the edge when Cr is absent. However, someone may argue that trapping could occur for the non-Cr edge if the incident power is reduced for the non-Cr edge. Actually in the experiment, no trapping is achieved for the non-Cr edge case even the incident power is extremely reduced. It indicates that a Cr thin film also affects the lateral confinement. To understand the difference caused by inducing the Cr planar thin film, near-field scanning optical microscopy is carried on to measure the transmitted intensity profiles of gold stripes sitting on glass slide with and without a Cr thin film. The intensity has been normalized by the transmitted power for each structure in order to fairly compare both structures. The transmitted power is obtained by averaging the site power measured at far from the edge, and dividing the entire power map by this average number. Figure 13 show the normalized transmitted power for structures without and with a Cr thin film, respectably. The slope of the first fringe is calculated from the first peak and valley by using the equation $(|\langle S\rangle|_{max} - |\langle S\rangle|_{min})/(x_{max} - x_{min})$ (see Fig. 13 (c)). To reveal the trends, the slope data are further smoothed

by FFT filter method for the structures with (red) and without a Cr thin film (black). The comparison of the slope for both structures is shown in Fig. 13 (d). It clearly shows that the lateral gradient is weakened when the Cr thin film is absent.

Although the purely electromagnetic analysis of the diffraction pattern can explain our observations, other additional effects such as photophoresis effect could be involved. Photophoresis force is caused by temperature gradient due to metal absorption of laser energy [63, 64]. Compared the edge structures with and without a Cr planar thin film, the temperature gradient and the induced photophoresis force are different. This also indicates that a Cr planar thin film may play a role in the trapping performance by a metal edge structure.

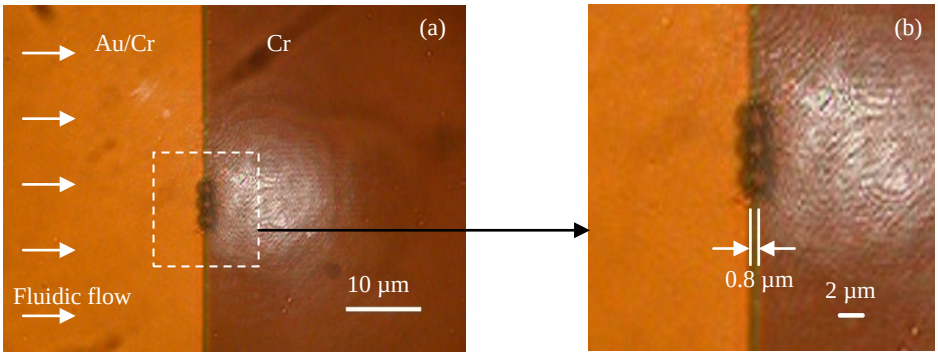

Figure 11. Trapping microspheres by an Au/Cr edge. (a) Three 2-µm-diameter PS microspheres are trapped when they are driven close to the edge by fluidic flow. (b) Magnification of the rectangular area shows that microspheres are trapped at 0.8 µm away from the edge.

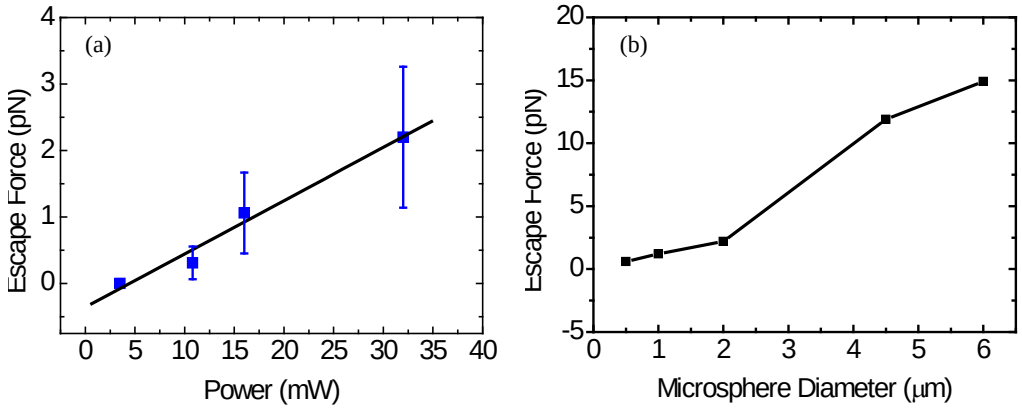

Figure 12. Escape force for a microsphere trapped by an Au/Cr edge trapping. (a) Escape force for a 2-μm-diameter trapped PS microsphere as a function of the incident laser power. (b) Escape force as a function of the microsphere diameter for incident laser power of 32 mW.

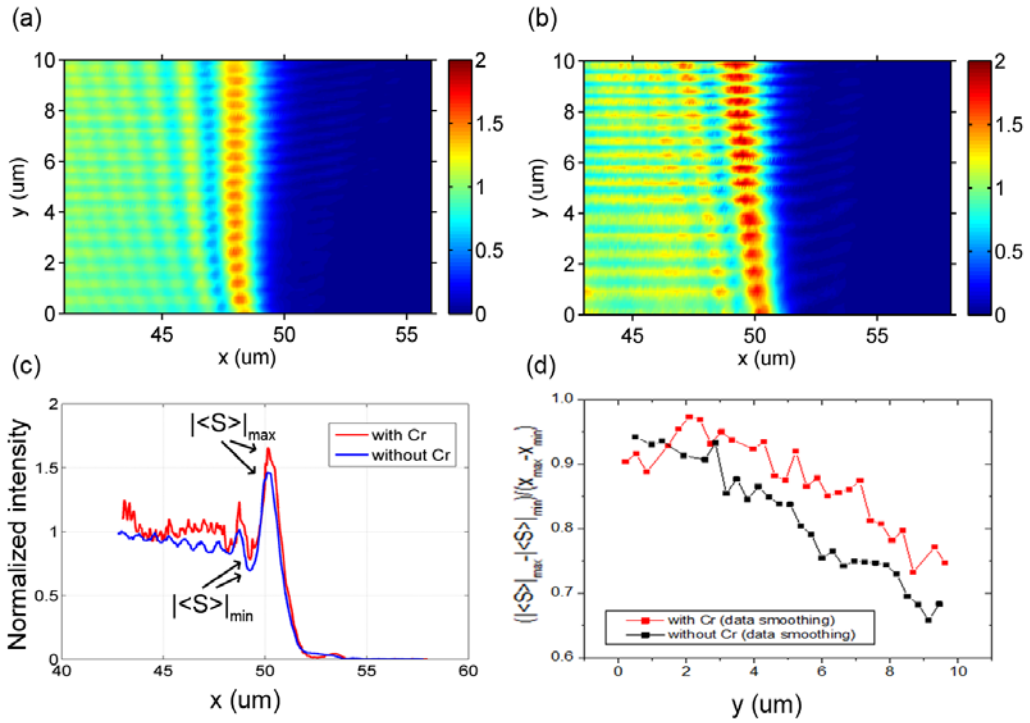

Figure 13. Transmitted beam profile around a gold stripe with/without a Cr planar thin film. (a) Normalized transmitted beam profile with a gold stripe without a Cr planar thin film measured by near-field scanning optical microscopy. (b) Normalized transmitted beam profile with a gold stripe with a Cr planar thin film measured by near-field scanning optical microscopy. (c) Comparison of the beam profile of both cases at y = 0.5 μm. (d) Slope calculated by (|<S>|max – |<S>|min)/(xmax – xmin) along vertical direction (y)for the structures with Cr thin film (red with symbol) and without Cr thin film (black with symbol). To get the trends, the data are smoothed by FFT filter method for the structures with Cr thin film (red) and without Cr thin film (black).

3.4 DUAL/MULTIPLE TRAPPINGS FOR MICROTUBULE DYNAMICS STUDY

A mitotic spindle is a highly ordered and dynamic macromolecular machine, responsible for accurately segregating chromosomes in cell division. Errors that occur during this process can result in cell death or a cancer. In vivo studies suggest that the machinery mechanics of spindle relies mainly on the microtubule polymerization or the action of molecular motors. Whereas it is difficult to study the individual roles of molecular motors and microtubules in living cells due to the enormous complexity of the system, in vitro studies have been performed to investigate roles of microtubules and molecular motors separately. In vivo studies of the dynamics of microtubules in mitosis and related movement show that assembling microtubules generates a pushing force and disassembling microtubules generates a pulling force [65]. A single microtubule assembled from purified tubulin molecules interaction with a rigid barrier can resist force of 3-4 pN [28, 66]. The dynamic instability of microtubules thus provides position strategies for a microtubule-organizing center through the cell, analogous to the centering of the nucleus of cells [65, 67, 68]. Functions of motor proteins such as Eg5, tau proteins and MCAKs in spindle also have been widely studied. Eg5 (the Kenesin-5 subfamily), which has anti-parallel arrangement of heavy chains configured like a ‘dumb-bell’, is essential for bipolar organization of mitotic spindles by crosslinking and sliding overlapping interpolar microtubules [69, 70, 71]. Tau proteins and MCAKs were found to regulate the dynamic behavior of microtubules [72, 73]. It is clear now that the different behaviors of microtubules during mitosis are due to the different cooperation with motor proteins, and the different structures that their ends engage with, which contain different microtubule-associated proteins. To fully understand the physical mechanism of cell division, it is essential to study not only the individual behaviors of microtubules but also their interaction with motor proteins *in vitro*.

Figure 14 (a) shows a theoretically calculated lateral force profile of a 1-μm diameter polystyrene microsphere at 1 μm above the metal edge. The force is calculated by ray optics model assisted with the FDTD simulated electric field. The balance position, where lateral force is zero, is at x = -0.95 μm. Any displacement along the positive x direction relative to the balance position will cause a restoring force. Between x = -1.2 μm and x = -0.2 μm, lateral force is proportional to the displacement. If the trap is calibrated, the force can be measured by monitoring the displacement.

When two metal edges are placed close to each other, it is possible to create a dual-trap or multiple-trap system by a single incident beam. Figure 14 (b) illustrates the desired configuration of dual traps. Two traps are several microns apart and each trap is designed to constraint one microsphere. The edges serve as tracks and microspheres can only move along the metal edge due to the lateral confinement. In this section, we demonstrate trapping multiple microspheres by a patterned Au/Cr edge and synthesis of microtubule bio-linked microspheres. We also discuss the potential of the dual-trap systems for microtubules dynamics and mitotic spindle mechanism study.

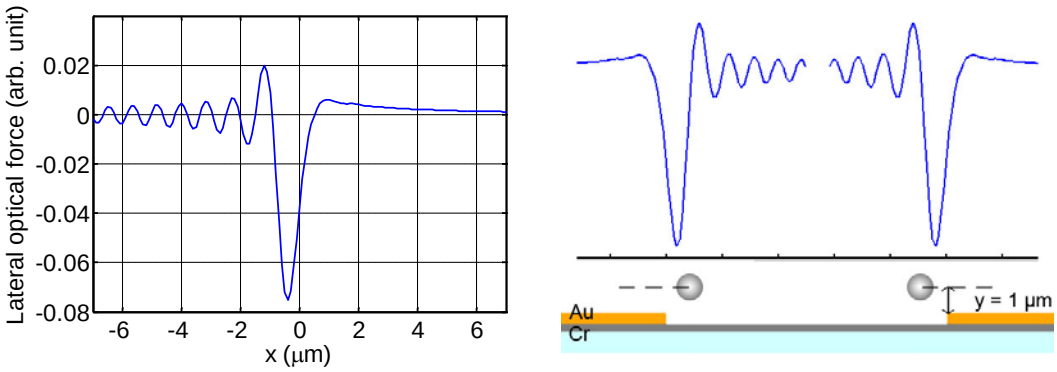

Figure 14. Schematic of a dual-trap system created by two close metal edges with two confined microspheres.

3.4.1 Fabrication and experiment

The gold edge patterns are fabricated on a glass slide by thermal evaporation and photolithography processes, followed by a lift-off process. A planar Cr layer of 10-nm thickness is first thermally evaporated on a clean glass slide. Photoresist (SC1805: S1027 = 1:1) of 1.2-μm thickness is then spin-coated on the Cr surface. By using the photolithography technique, PR patterns are formed on the Cr surface. Gold is then thermally evaporated on the PR patterns. The thickness of gold is about 110 nm. After a lift-off process in acetone, the structure of Au patterns on a planar Cr is formed. A cover slip flow cell is constructed by a glass cover slip adhered to the substrate with metal edge pattern by two pieces of double-sided clear tape (75 μm high), the pieces of tape separated to form a channel approximate 5 mm wide. To achieve optical trapping, a diode pumped solid-state laser (λ = 1064 nm, B&W Tech) is used as the laser source. While a collimated input laser beam is sufficient to form a trap, a 10× DIN objective (0.25 NA) is used to enhance the intensity of a laser beam (the maximum output power available from the laser is 50 mW). The incident laser power was measured to be 32 mW. The laser spot illuminated at the metal/water interface has a diameter of about 50 μm. The corresponding intensity is calculated to be 2×10^7 $W \cdot m^{-2}$.

Tubulin and buffer are purchased from Cytoskeleton Inc. Rhodamine-labeled tubulin, biotin-labeled tubulin and unlabeled tubulin were provided as lyophilized power. Before use, they were first reconstructed by dissolving in PEM buffer (80 mM Na–PIPES [piperazine-N,N-bis (2-ethanesulfonic acid)] (pH 6.9), 1 mM $MgCl_2$ and 1 mM EGTA [ethylene glycol bis(beta-aminoethyl ether)- N,N,N',N'-tetraacetic acid]) with 1mM GMPCPP (Jena Bioscience GmbH, Germany). Rhodamine tubulin was prepared in 50 μM (5 mg/mL) and biotin tubulin was 5 μM (0.5 mg/mL). 2 μL 50 μM rhodamine-labeled tubulin was incubated on ice for 5 min and then

was transferred from the ice to a 37^{o}C water bath and incubated for 20 min. 5 μL 0.5 μM biotin tubulin was added into the tube. The mixture was incubated for another 20 min. In this step, short GMPCPP-stabilized seeds were formed and the length of these seeds was about 1 - 2 μm. At the end of the incubation of the mixture of rhodamine tubulin and biotin tubulin, 100 μLPEMT (PEM with 10 μM taxol) was added into the mixture and gently mixed. The microtubule solution was transferred to a 1.5 mL micro tube and was centrifuged at 13000 rpm for 60 min (15 min x 4). The supernatant was discarded and the pellet was suspended in 5 μL PEMT. To bind MTs to the streptavidin-coated microspheres (Bangs Laboratory), the microtubules were first washed using a centrifugation method. 5 μL microspheres stock solution was transferred into a 1.5 mL micro tube. 10 μL PEM was added and the tube was centrifuged at 5000 rpm for 15 min. After removal of the supernatant, the pellet was resuspended in 20 μL PEM. Before binding the functional MTs to microspheres, the microspheres were centrifuged again and then the pellet was suspended in the 5 μL washed microtubules. The mixture was gently mixed and left at room temperature for at least 20 min before use. The microtubules depolymerized continuously after assembly. Therefore the solution was used within 3 days.

Microtubule samples were observed by a modified fluorescence microscope. A 532 nm diode pumped solid state laser was used as the light source. A laser beam was aligned and incident from epi-fluorescence port and illuminated to the sample by the objective (40x Plan, N.A.0.65). This objective also collected the excited red fluorescence light. The emitter filters have center wavelength of 580 nm and FWHM of 10 nm. The fluorescence images of the specimen were taken by a digital CCD camera (Nikon coolpix 995). The exposure time of the camera was about 8 seconds. Contrast in the fluorescence images was further enhanced by averaging and background subtraction performed by Photoshop.

3.4.2 Results

Microspheres driven by fluidic flow are captured by edge traps when they move closer to the edge. Once the microspheres are trapped, they stay at the same position unless the fluidic flow increases larger enough to force the microsphere escape from the edge. For a 1-μm-diameter PS microsphere at incident power of 32 mW, the escape velocity normal to the edge is 62 μm/s. Using the modified Stokes's theorem [5, 31], the drag force, which is equal to the escape force, is calculated to be 1.2 pN with the assumption that the gap between the bottom of microsphere and the metal surface is 100 nm and the speed of fluid flow is same as the speed of the escaping microsphere. At incident power of 32 mW, the escape forces for a 2-μm-diameter and a 6-μm-diameter PS microsphere are also measured, which are 2.2 pN and 14.9 pN respectively.

The capture efficiency of microspheres depends on the concentration of microspheres and it also varies from different metal patterns. Figure 15 shows microspheres trapped by three Au/Cr patterns. The chance of trapping of microspheres is relative higher for metal patterns that cover mostly by gold, which is shown in Fig. 15 (a) and Fig. 15 (c). It can be explained in that the transmitted power of the incident laser beam is strong at the area without Au. The forward scattering force pushes the microspheres away from the metal surface and edge, which means that the chance of microsphere approaching metal edges is less. In Fig. 15 (a), two 2-μm-diameter microspheres are trapped at the outer circumference and the distance is 26 μm, while two 6-μm-diameter microspheres are also trapped at the outer circumference and their distance is 17 μm. It also should be noted that a quadrant pattern enhances the trapping chance and also help microsphere position in proper distance. This is due to the illumination area limit of the incident laser beam. As shown in Fig. 15 (c), three 1-μm diameter microspheres are trapped and are aligned along each side of the quadrant with distance ranging from 21 μm to 24 μm.

The assembled microtubules in the presence of GMPCPP are shown in Fig. 16 (a). The length of these MTs is about 10 μm. Most microspheres have more than 5 MTs attached around. Fluorescence image of the assembled AMOCs in the presence of GMPCPP was shown in Fig. 16 (b). Since the microspheres themselves contain no fluorophore, the bright orange fluorescence emitted from the microspheres comes from the free biotin-labeled tubulin and biotin-labeled tubulin cooperated in the microtubule lattices, confirming that the binding between biotin and streptavidin. Some dots, which were brighter than others, were shown to be clusters of microspheres by comparison between the fluorescence image and the corresponding bright field image. These clusters of microspheres may be due to the tendency of accumulation of small particles or they may linked by biotin-labeled microtubules.

Higher magnification images of the AMOCs are shown in Fig. 16 (c). The structures of AMOCs extracted from the fluorescence images are sketched at the right column (Fig. 16 (d)). It is clear shown that aster structures were formed in the presence of GMPCPP. A microsphere was attached with 2-5 MTs and these MTs were all radially expending outward. The number of attached microtubules can be controlled by adjusting the relative concentration of the microspheres to the microtubules. The length of the MT can be controlled by dilution ratio during the step when adding PEMT to MT seeds. At low dilution ratio (< 20X), the length of MTs seeds is about 3 μm and does not change much when the dilution ratio increases from 2.5X to 20X. The length increases dramatically to 20 μm at 500X dilution and decreases a little at 1000X dilution (13 μm).

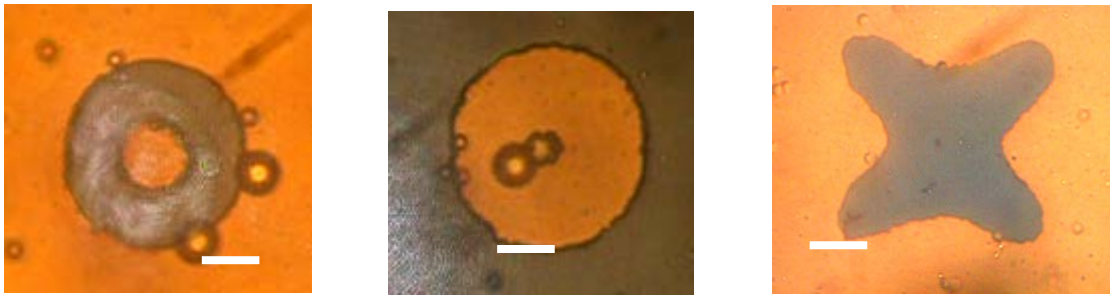

(a) (b) (c)

Figure 15. Microspheres are trapped by Au/Cr patterns. (a) Two 2-μm diameter microspheres and two 6-μm diameter microspheres are trapped simultaneously by a ring pattern. (b) Two 2-μm diameter microspheres are trapped closely by a disc pattern. (c) Several 1-μm diameter microspheres are trapped by a quadrant pattern. Bars: 10 μm.

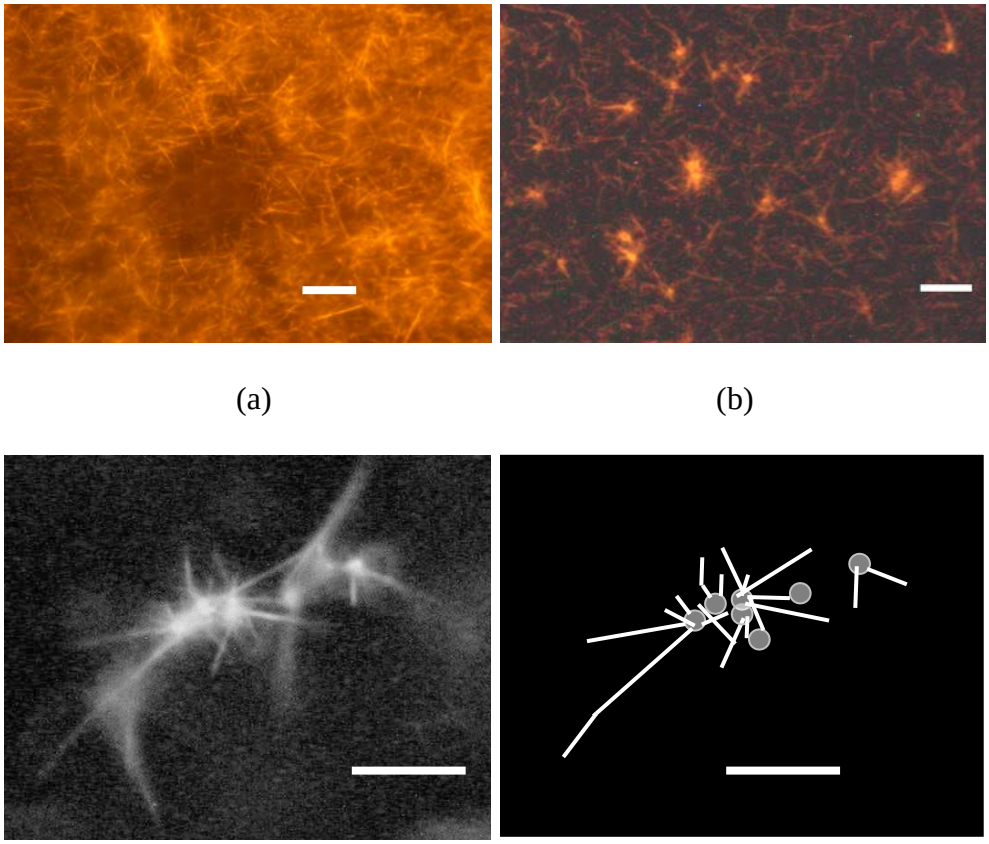

Figure 16. Microtubules and AMOCs. (a) Microtubules before assembly of AMOCs. (b) AMOCs assembled with GMPCPP by 1-µm diameter streptavidin-coated polystyrene microspheres. (c) Multiple MTs are packed around each discrete microsphere forming AMOCs. (d) Sketches of the structure simplified from (c). Bars in (a) and (b) are 20 µm. Bars in (c) and (d) are 5 µm

3.4.3 Discussion and conclusion

Using a patterned metal edge structure, multiple trapping can be achieved by a single incident laser beam. The distance between two trapped microspheres is random because it depends on the concentration of microspheres and how the microspheres driven by the fluid to the metal edges. Precise position of microspheres on the metal edge can be done by using a steering optical tweezers. Once two microspheres are trapped by metal edges, the distance between them is constant unless the external force is changed. Assembled AMOCs are microspheres biologically linked with microtubules. The length of outward microtubules can be adjusted by diluted ratio of buffer solution to the seeds. When two AMOCs are trapped by the integrated Au/Cr edge traps and separated at a proper distance, the microtubules of each microsphere overlap. This “apparatus” mimics the basic structure of mitotic spindle.

In summary, trapping of two or more microspheres by a patterned metal edge with a single incident laser beam is demonstrated. AMOCs that microspheres biological linked with microtubules are assembled. When microspheres in the dual-trap system are replaced by AMOCs, it can be turned into an “apparatus” that two AMOCs with their microtubules act as a scaffold for proteins, meanwhile, optical trapping by the metal edges serve as tracks and also provide force measurement. This “apparatus” has the potential for use in studying microtubule dynamics and interactions of proteins and microtubules.

3.5 PARTICLE SORTING BY AU/CR EDGE TRAPPING

Optical trapping has been widely used in biological, microfluidic and physical areas because it is a noncontact, noninvasive and precise method for manipulation of objects in solution on the microscopic scale. A major interest in implementation of optical trapping within microfluidic systems arises from the needs to manipulate and separate cells. Several spatially distributed optical trapping techniques have been reported to generate linear optical trapping for microscale separations within flowing systems. These techniques include using a fiber-focused diode bar [50], rapidly scanning a single beam [51, 52, 53], or using holographic array generators [54]. These methods either involve modified laser source, sophisticated steering hardware with software control, or extra external optical components.

In this section, we present a simple approach based on metal edge trapping that allows dielectric microspheres separations within flowing microfluidic systems. Our scheme takes the advantage of the feature of metal edge trapping which converts a uniformly distributed incident light to a linear geometry along the metal edge.

Au/Cr stripes are fabricated by using photolithography, thermal evaporation and lift-off method. The substrate with Au/Cr stripes is caged in a PDMS microfluidic channel having both an inlet and an outlet. The channel is 75-μm high and 2-mm wide. The angle between the flow direction and the gold edge (θ) will be change in the experiment (Fig. 17 (a)). To adjust this angle, the flow cell is disassembled and then PDMS is then peeled off, realigned and reattached to the substrate. Polystyrene latex microspheres of 2 μm and 6 μm diameters are mixed in 0.5 mg/mL BSA aqueous solution and are injected into the PDMS channel. The flow rate is controlled by adjusting pulling speed of the syringe. Videos of the PS microsphere movements around the gold edge are taken by a CCD camera (Nikon Coolpix 995) in 15 fps through the

Nikon Microphot microscope. A 40× micro objective is used to observe the motion of microspheres around the gold edge. The diode pumped solid-state laser with wavelength of 1064 nm is used as the laser source. The 10x objective is also used to enhance the beam intensity. The effective incident power is fixed at 32 mW.

The redirection of microspheres is affected by the fluidic flow rate and the angle θ. At a fixed angle, the result shows that microspheres pass the edge without changing the direction if the incident velocity is sufficient high. When incident speed slow down to a certain level, the drag force is balanced with the component of the trapping force along the flow direction, microspheres remain within the edge trap and are guided along the edge until they move out of laser effective illumination spot. The angle to efficiently separate two sizes of microspheres is tested to be 55 degree. Figure 17 (b) shows the pathways of two different size microspheres that are being redirected when passing through the gold edge at an incident angle of 55 degree. The flow rate is about 16 μm/s. Most microspheres of 2 μm size (blue) are redirected and move along the edge for about 27 μm and then released where the laser power decreases. In contrast, the 6 μm diameter microspheres pass the edge without significant change of direction. Within the laser effective trapping region, about 50 percent of 2 μm diameter microspheres are redirected by the edge. Although larger beads experienced greater trapping forces than smaller beads, its equilibrium *x* position goes further into the blank area. Larger microspheres also experience larger forward scattering force. This may lead to less strong confinement in the lateral direction for larger microspheres. Sorting microspheres according to their size is expected to be possible by using a single gold edge.

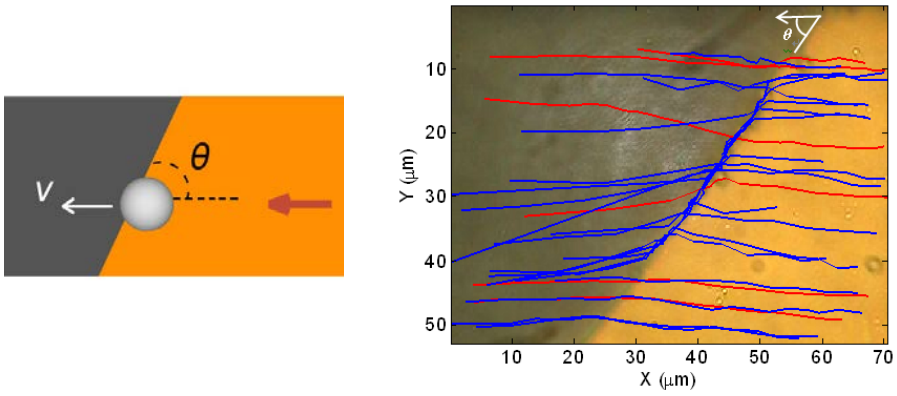

(a) (b)

Figure 17. Traces of PS microspheres with diameter of 2 μm (blue) and 6 μm (red) when microspheres pass a gold edge trap.

3.6 SUMMARY

We presented a simple and easy-to-implement 2D optical trapping based on diffractive transmission of light around an Au/Cr edge structure. Trapping of multiple polystyrene microspheres around the edge are achieved by a single incident laser beam. We also developed a model to theoretically calculate the optical trapping force. The predicted optical trapping force is at the order of several pico Newtons, as supported by the measurement result. This trapping force is comparable to those of traditional optical tweezers. This new optical trapping structure is polarization-independent and can operate with normal incident laser beam of relative low power. It offers a promising potential in view of the demand of incorporating a trapping function into the on-chip system. In addition, the edge trapping approach has advantages over other methods in many aspects: simplicity of fabrication, low cost, polarization-independence and minimal requirement on external optics.

To demonstrate the utility of metal edge trapping, we designed metal patterns to create dual/multiple-trap systems with AMOCs. The microsphere of AMOCs can be used as a handle for each optical trap. Once the two optical traps are calibrated, the force can be measured in real time. This system can be a potential tool for study of microtubule dynamics and protein interaction with microtubules.

We also directly integrated the optical control into microfluidic systems to present an easy implementation of metal edge trapping for microspheres separations within flowing microfluidic systems. The results demonstrate different sizes of microspheres can be separated within microscopic scale by use of a metal edge and a single incident laser beam.

4.0 INTERACTIONS OF RADIOFREQUENCY WAVES WITH GOLD NANOPARTICLE COLLOIDAL SOLUTIONS

Metal nanoparticles (NPs) possess interesting thermal properties that are potentially useful in a wide range of applications. Illumination of metal NPs at proper wavelengths, for example, can result in local deposition of heat in a nanoscale confined space. This photo-thermal conversion effect in metal NPs has been extensively investigated for bio-imaging and detection, remote release of drugs, and treatment of diseases [12, 13, 14, 15, 16, 17, 18, 19]. Besides the energy conversion capability, metal-NP-containing fluids have also been reported to demonstrate improved heat-transfer properties of liquids [74]. The underlying mechanism of photo-thermal conversion commonly involves surface plasmon resonance in metal NPs. Surface plasmons, collective oscillations of electrons under optical excitation, show strong absorption of light around the resonance wavelength (e.g., ~530 nm for gold NPs) [12, 13]. Proper design of the size and shape of a metal nanoparticle can shift the plasmon resonance to longer wavelengths. A gold nanoshell structure, for example, shows resonance absorption at near-infrared (NIR) wavelengths [18]. While this longer-wavelength operation alleviates radiation damage, the penetration depth into a body in the optical frequency range is relatively small (2-3 cm at NIR wavelength). In most *in-vivo* applications it is highly desirable to maximize the energy-absorption contrast between nanoparticles and media (body/tissue).

Use of radiofrequency (RF) electromagnetic waves as an energy source for possible thermal-conversion in metal NPs potentially offers a unique advantage over the photo-thermal conversion. Compared to the case of optical waves, RF waves can transmit through a body with

negligible absorption, e.g., penetration depth of 20-200 cm at 13.56 MHz, and this transparency renders RF waves more bio-safe than lasers [75]. Use of metal NP colloidal solutions in conjunction with RF waves has therefore been drawing attention as a possible means to deposit heat in a local confined space for RF ablation of cancer [21, 22, 23, 24]. The assumption commonly taken in these experimental works on RF exposure of Au-NP-containing solutions is that Au-NPs efficiently absorb incident RF energy via Joule heating. This underlying assumption of RF-to-thermal conversion in metal NPs, however, has not been unambiguously tested yet, and a clear physical understanding needs to be developed before exploring the full potential of the subject phenomenon. Considering the electrolyte nature of Au-NP colloidal solutions, the ionic constituents (mono- or polyatomic ions from the solutes dissolved into the solvent) may potentially offer different pathways to absorbing incident RF energy [76].

In this study we have quantitatively measured RF-induced heating in gold nanoparticle colloidal solutions. The possible role of Au NPs in RF energy absorption was scrutinized in this work by employing properly designed control samples. Au NPs were physically separated from the colloidal solutions by centrifugation. RF testing of thus-separated solutions (the supernatant and the Au-NPs resuspended in de-ionized water) clearly reveals that Au NPs do not contribute to RF-to-thermal conversion. The AC conductivity measurement of the colloidal solutions with and without Au-NPs confirms that the ionic conduction under RF fields causes Joule heating in the electrolyte solutions.

4.1 MATERIALS AND METHODS

The Au nanoparticle colloidal solutions used in this study were purchased from Ted Pella, Inc.: #15702-20 (5-nm-diameter Au NPs at $5.0x10^{13}$ particles/cm^3 concentration); #15703-20 (10 nm at $5.7x10^{12}$ cm^{-3}); #15705-20 (20 nm at $7.0x10^{11}$ cm^{-3}); #15708-20 (50 nm at $4.5x10^{10}$ cm^{-3}); #15711-20 (100 nm at $5.6x10^{9}$ cm^{-3}); #15713-20 (200 nm at $7.0x10^{8}$ cm^{-3}) **[**77]**.** In order to separate Au NPs, the colloidal solutions were centrifuged (Hettich Zentrifugen MIKRO12-24) at 13,000 rpm for 15-30 min. The supernatant part was taken away from the tube, and the pellet part in the bottom was resuspended by adding de-ionized (DI) water and performing sonication (Fig. 18).

NP separation by centrifugation was characterized by optical extinction measurement. The characterization setup consists of an optical spectrum analyzer (B&WTek BRC111A: spectral range of 350-1050 nm; resolution of 2 nm), a white light source (B&WTek BDS100: 5-W-deuterium/3-W-tungsten lamp source; 200-1100 nm), and a fiber-coupled (1000-μm core diameter) cuvette holder (B&WTek BCH100). A clear plastic tube (Daigger Microcentrifuge Tube 0.6 mL) that contains 0.5-mL colloidal solution was placed in the cuvette holder for measurements in a transmission mode. The spectra of optical transmission through a sample contain information on the extinction (absorption and scattering) characteristic of the colloidal solution. The transmission through a microtube with DI water only was also measured and used as a reference in calculating optical transmission of colloidal solutions, and thus extinction spectra.

The NP-separated solutions (the supernatant part that contains most background ions, and the resuspended Au-NP solutions in DI water) and the original stock solutions were tested for

possible RF absorption. RF heating experiments were performed at 13.56 MHz at 25 W power (electric field strength of 2.5 kV/m). Each solution (0.5 mL) contained in a microtube was placed in between the transmission and reception heads of a RF generator (Therm Med LLC Kanzius machine) [22, 78]. This generator consists of a power source coupled to the transmission/ reception heads that are arranged in the co-axial end-fired configuration. The electric field strength generated between the two heads was measured in a Faraday-shielded room at low powers using an isotropic field probe and monitor (Amplifier Research FP2000 and FM2004). A spectrum analyzer (Agilent 8566B) was connected to the system to accurately measure transmitted power. At 5 cm from the transmission head with head spacing of 30.5 cm, the electric field strength is estimated to be 2.5 kV/m (the composite field strength calculated by taking the square root of the sum of the field squares measured along the three axes) at 25 W transmitted power. The temperature of the solutions was monitored with a fiber-optic temperature probe (LumaSense Technol. LUXTRON 812 Thermometer with STB Probe) immersed into the colloidal solution. The sensor tip of the fiber-optic probe was positioned at the middle of liquid column height, touching the inner wall of the plastic tube (Fig. 19).

The electrical conductivity and dielectric constant of colloidal solutions were characterized by measuring the complex impedance of a cell containing a liquid sample. The liquid cell is defined by two parallel plate electrodes (200-nm-thick Al films deposited on glass substrates) of 4 mm x 4 mm electrode area and 530 μm gap. By changing the ratio of electrode area to gap size, the cell impedance level can be adjusted into proper ranges compatible with the measurement instruments employed. The liquid cell was serially connected to an external resistor of predetermined value. The circuit was then driven by a sinusoidal signal (1 V peak-to-peak; variable frequency in the range of 10 Hz to 20 MHz) from a function generator (Agilent

33220A), and the amounts of voltage division and phase change between the two components were measured using an oscilloscope (HP54603B). The cell impedance was then calculated from the measurement result obtained with this voltage divider circuit. The complex impedance of a cell containing electrolyte solution can be equivalently represented by a series combination of the electrical double-layer capacitance (C_{DL}) and the impedance of the liquid itself (Fig. 23) [79]. The double-layer capacitance is associated with the liquid-electrode interface. The AC current conduction in an electrolyte solution usually involves two different mechanisms, transport of mobile charges (ions) and displacement and/or rotation of polarization charges at the molecular level. The liquid admittance (inverse of impedance) can then be further represented by a parallel combination of the ionic conductance (G_{EL}) and the dielectric capacitance (C_{EL}) of electrolyte solution. At low frequencies the serially connected double-layer capacitance part dominates the overall cell impedance. At high frequencies the impedance of the double-layer capacitance part becomes negligible, and the liquid impedance itself determines the cell impedance. From the measured impedance values and the information of cell dimensions, the capacitance (C) and conductance (G) values were extracted. The electrical conductivity (σ) and dielectric constant (ε) of electrolyte solutions were then calculated referring to the formula, $Y = G + i\omega C = (\sigma + i\omega\varepsilon)A/L$, where ω is the angular frequency, and A and L represent the cell electrode area and gap, respectively.

Presence of various ionic elements remaining in Au-NP colloidal solutions was tested by performing a transmission electron microscopy (TEM) study with JEOL JEM-2100F scanning TEM equipped with Oxford INCA energy dispersive X-ray spectrometer (EDS). TEM specimens were prepared by placing a drop of the solution (50-nm Au-NP stock solution or the supernatant)

onto holey carbon coated Cu grids and dried in air. The specimens were loaded into the electron microscope and examined at bright-field TEM mode and STEM mode (Fig. 24).

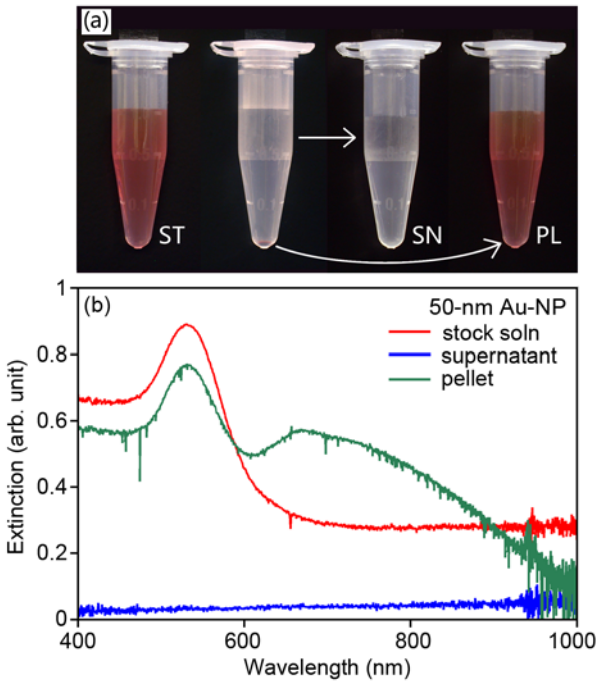

Figure 18. Separation of gold nanoparticles by centrifugation. (a) 50-nm Au-NP stock solution (ST); after centrifugation (second from the left); supernatant (SN); resuspended pellet solution (PL). (b) Extinction spectra confirming Au-NP separation after centrifugation.

4.2 RESULTS AND DISCUSSION

Au-NP colloidal solutions of various different particle size and concentration were tested in this work: 5-nm-diameter Au NPs at $5.0x10^{13}$ particles/cm^3 concentration; 10 nm at $5.7x10^{12}$ cm^{-3}; 20 nm at $7.0x10^{11}$ cm^{-3}; 50 nm at $4.5x10^{10}$ cm^{-3}; 100 nm at $5.6x10^{9}$ cm^{-3}; 200 nm at $7.0x10^{8}$ cm^{-3}. Note that the six colloidal solutions contain the same amount of Au at $6x10^{-3}$ wt % level. Figure 18 shows the result of NP separation by centrifugation in 50-nm Au-NP colloidal solution and the measured extinction spectra. Whereas the Au-NP-containing stock solution shows characteristic red-brown color, the supernatant is clear and transparent. The resuspended pellet solution that contains centrifuged Au NPs shows red-brown color, the same as the original stock solution. The stock solution shows a well-defined peak at 530 nm, which corresponds to Au-NP surface plasmon resonance [12, 13]. The pellet solution also reveals the same plasmon resonance peak at 530 nm, but with slight reduction in peak height. Appearance of a shoulder at the longer wavelength side (around 700 nm) of the peak indicates formation of Au-NP clusters. The synthesis of Au-NP colloidal solutions involved citrate ions that are designed to stabilize nanoparticle surfaces against aggregation [77, 80, 81, 82]. The nanoparticle aggregation in the pellet solution, as evidenced by the appearance of the shoulder, can be understood in view of the fact that the pellet part is significantly diluted with DI water after separation by centrifugation. Au NPs are then expected to become less stabilized because of reduced citrate concentration, therefore more prone to aggregation. In a drastic contrast, the supernatant does not show any measurable extinction in the entire spectral range. Overall this nanoparticle-separation by centrifugation is confirmed to work well for particle sizes down to 20 nm, as tested by extinction measurement.

Figure 19 shows the measurement result of RF heating of 50-nm Au-NP colloidal solution: the stock solution (red curve), the supernatant part of centrifuged solution (blue), and the pellet solution containing centrifuged Au NPs (green). The stock solution shows a temperature rise of ~0.3 ^{o}C/s at 25-W RF power. It is interesting to note that the supernatant also shows the same rate of temperature rise as the stock solution. By contrast the Au-NP-containing pellet solution shows only an insignificant level of heating at ~0.003 ^{o}C/s. This result clearly reveals that Au-NPs do not contribute to RF energy absorption. As a reference for background absorption, DI water was also tested under the same RF exposure condition. It is well known that pure water does not absorb incident electromagnetic energy well at this frequency range [83]. The measurement result shows a similar heating rate as that of the pellet solution case, confirming negligible absorption of RF energy at the given level of incident power. Figure 19 (c) shows a summary of the results from the solutions with different particle sizes (for clarity, only 20, 50, and 200 nm diameter cases are shown). Regardless to particle size, all stock solutions show the same heating rate as the supernatant solutions, and all pellet solutions produce negligible heating (at least two orders of magnitude smaller than the stock solutions). Overall this RF exposure experiment unambiguously demonstrates that Au NPs did not contribute to the observed RF heating of Au-NP colloidal solutions.

In order to corroborate the observation that Au NPs do not show any RF absorption but the supernatant does, additional experiments were designed and carried out: the same Au-NP stock solutions (50-nm-diameter NPs at $6x10^{-3}$ wt % concentration) were separated into supernatant and pellet parts via centrifugation. This time the supernatant part was further diluted to x1/3 or x1/6 concentration level by adding different amount of DI water. The Au-NP pellet part was resuspended into DI water at three different concentrations: x1, x3, and x6. Here the x1

pellet solution corresponds to the same Au-NP concentration as before, and the x3 and x6 solutions represent 3 or 6 times higher concentration, respectively, compared to the reference (x1) solution. As the NP concentration is increased, the characteristic red-brown color becomes thicker (Fig. 20 (a): resuspended Au-NP pellet solutions at three different concentrations). The optical extinction measurement confirms clear separation of Au NPs from the colloidal solution (Fig. 20 (b)): No absorption or scattering peak that can be attributed to presence of Au NPs is found from the extinction spectra of three supernatant solutions. By contrast, the resuspended pellet solutions show stronger absorption and scattering as the Au NP concentration is increased.

RF heating experiments were performed on the six solutions under the same RF condition as before (Fig. 21: global profiles of temperature change measured up to 30 min). Upon exposure to RF wave, the three supernatant solutions showed a steep rise of temperature with different slope. In contrast, the three Au-NP pellet solutions showed only a negligible amount of temperature rise for the same duration of RF exposure. The initial parts of the temperature rise profiles of six solutions are shown in Fig. 22. The supernatants show slopes of 0.275 ^{o}C/s, 0.089 ^{o}C/s, or 0.043 ^{o}C/s for x1, x1/3, or x1/6 dilutions, respectively (Fig. 22 (a)). The excellent linear relationship between the measured slopes and the dilution suggests that RF energy absorption in the supernatant solutions is determined proportional to the ionic concentration of solution. By contrast, the Au-NP pellet solutions show slopes of 0.0029 ^{o}C/s, 0.0043 ^{o}C/s, or 0.0046 ^{o}C/s for x1, x3, or x6 concentration, respectively (Fig. 22 (b)). Unlike the supernatant case, no clear relationship is observed between the measured slopes and the Au-NP concentrations. Note also that a RF testing of DI water without any ionic solution or Au NPs showed a residual amount of temperature rise, estimated to be ~0.003 ^{o}C/s as discussed above. The insignificant level of temperature rise of the pellet solutions is attributable to possible presence of a residual

concentration of ions in the solutions, which might be contained in the pellet part during separation of the supernatant part after centrifugation. Overall the results of this additional experiment clearly show that the amount of RF heating is proportional to the ionic concentration of background solution and that Au NPs do not make a contribution to RF energy absorption.

In the early stage of heating, the slope of temperature rise is determined as Q/C_pM, where Q is the total heat generation rate, and C_p and M are the heat capacity and the mass of colloidal solution [19, 84] From the measured slope of temperature rise (~0.3 ^{o}C/s for the case of original stock solutions and undiluted supernants) and the volume, density and heat capacity information of water (0.5 mL; 1 g/mL; 4.18 $Jg^{-1}K^{-1}$) [83, 85], the total heat generation rate Q in the solution column is estimated to be ~2 W for both stock and supernatant solution cases. The observation that Au NPs do not contribute to RF energy absorption can be understood in view of the fact: the metal (Au) has high conductivity (σ = 5x10^7 S·m^{-1}) [83], and electrons abundant in a metal NP quickly compensate incident electric field so that the electric field inside the metal becomes negligible. The RF magnetic field can penetrate into metal (down to the skin depth range, ~10 μm at 13.56 MHz) [30] and can induce the rotational electric field inside the nanoparticle. Someone may argue that this induced electric field may contribute to Joule heating in conjunction with conduction electrons available in metal. A simple calculation (see below), however, shows that the amount of induction heating in a non-magnetic metal nanoparticle is many orders of magnitude smaller than what we have observed in this work.

The amount of induction Joule heating in a non-magnetic metal nanoparticle is expressed as $\frac{1}{30}\mu_0^2\sigma R^5\omega^2 H_0^2$ [36, 37, 38]. Here μ_0 is the permeability of free space, σ is the electrical conductivity of metal, and R is the radius of nanoparticle. ω is the angular frequency and H_0 is the magnetic field. For the case of a 50-nm Au-NP exposed to 13.56 MHz, 25-W RF power (H_0

= 1 A/m), the amount of heat generation is calculated to be of 10^{-28} W order. Considering the Au-NP concentration (4.5×10^{10} cm^{-3}), the total heat generation in 0.5 mL colloidal solution is estimated to be 10^{-18} W order. [We note that this calculation should be considered as 'order of magnitude' estimation, given the uncertainty in accurately measuring the magnetic field strength that Au NPs would experience.] This number is 18 orders of magnitude smaller than the heat generation experimentally observed in the present work (~2 W), and this analysis clearly confirms that the magnetically-induced Joule heating in Au NPs cannot account for the measurement result.

This characteristic feature of RF absorption in Au colloidal solutions, especially whose independence of Au-NP presence in the solution, can be understood in view of the electrolytic nature of Au-NP synthesis process: Au ions that are dissolved in an aqueous solution are neutralized and condensed to form nanoparticles by reduction chemicals introduced to the solution [80]. It is likely that there would be a significant amount of background ions that do not participate in Au NP formation but remain dissolved in the colloidal solution. These background ions drift in the solution driven by incident RF electric field. This ionic conduction process generates heat at the rate of σE^2 via Joule heating, where σ is the electrical conductivity of the electrolyte solution and E is the electrical field [30, 86]. The dielectric relaxation of polar water molecules can also cause heating in the microwave frequency range (~18 GHz), but this effect at RF frequency (13.56 MHz) is confirmed to be negligible as shown in Fig. 19. In order to substantiate the connection between RF heating and ionic conduction, the electrical conductivity of electrolyte solutions was measured using a liquid cell in conjunction with an impedance measurement technique.

The complex impedance of a cell with different liquid was measured at 10 Hz to 20 MHz: the equivalent circuit model of impedance (Fig. 23 (a)) [79]; the real part of cell admittance, Re[Y] (Fig. 23 (b)); the imaginary part of cell admittance, expressed as Im[Y]/ω (Fig. 23 (c)). The three solutions show the same tendency that in the low frequency range the admittance values are strongly frequency-dependent whereas in the high frequency range they remain at a constant level. Both the stock and supernatant solutions show almost the same admittance values (both real and imaginary parts) in the entire frequency range. In contrast the real part of the pellet solution's admittance in the high frequency regime shows distinctly smaller values than those of stock/supernatant solutions. The imaginary part of the pellet solution approaches the same level as those of two other solutions. The frequency dependence of cell impedance can be understood with reference to the equivalent circuit model shown in Fig. 23 (a). In the low frequency regime, the impedance of double layer capacitance (C_{DL}) dominates over the liquid (electrolyte) impedance. In the high frequency regime, the liquid impedance part determines the overall cell impedance. In the latter regime, the liquid admittance can be represented as a parallel combination of ionic conductance (G_{EL}) and dielectric capacitance (C_{EL}). The admittance values in the high frequency region (1 MHz – 20 MHz) were used in extracting the capacitance and conductance values, and from which the electrical conductivity and dielectric constant of liquid (Fig. 20 (d) and Fig. 20 (e)) [87]. The probe impedance (Tektronix P6122: 10 MΩ and 11 pF) and the parasitic/fringe capacitance associated with the liquid cell and its connection to instruments were also taken into account in this calculation. Both the 50-nm Au-NP stock solution and the supernatant show the same level of conductivity at $3x10^{-2}$ to $4x10^{-2}$ $S \cdot m^{-1}$, whereas the pellet solution reveals $5x10^{-4}$ to $2x10^{-3}$ $S \cdot m^{-1}$. This drastic difference (by a factor of ~30) in electrical conductivity correlates well with the heating rate difference observed in RF

exposure, that is, ~0.3 ^{o}C/s versus ~0.003 ^{o}C/s. Overall this AC conductivity measurement result confirms that the observed RF heating can be explained in terms of Joule heating associated with ionic conduction in electrolyte solution.

From the measured electrical conductivity and the information of ion mobility (~$2x10^{-8}$ $m^2V^{-1}s^{-1}$) [82], the total ion concentration of the stock or supernatant solution is estimated to be ~$9x10^{18}$ cm^{-3}. This corresponds to ~0.01 M concentration, and compares well with the level of total ionic concentration in original solution estimated from the recipe of Au NP synthesis, which involves ($HAuCl_4$ + sodium citrate + tannic acid + K_2CO_3 solutions) [77, 80, 81, 82]. The dielectric constants of the three solutions are estimated to be ~100, close to that of pure water, 78 at 13.56 MHz. This close match can be understood in view of the fact that the Au-NP concentration in the colloidal solution is at a relatively low concentration (~$6x10^{-3}$ wt %).

According to the equivalent circuit model of a liquid cell, the overall frequency-dependence of cell admittance can be characterized by two different time constants, $\tau_1 = C_{DL}/G_{EL}$ and $\tau_2 = C_{EL}/G_{EL}$ (or two cutoff frequencies, $1/\tau_1$ and $1/\tau_2$). In most liquid cells, the double layer capacitance (C_{DL}) is usually much greater than the liquid capacitance (C_{EL}). This is because the former is defined by charge separation narrowly confined to the electrode surfaces whereas the latter is mostly determined by the gap (separation) of electrodes. The real part of cell admittance (Re[Y]) becomes frequency-independent at > ~5 kHz for the stock and supernatant solutions case and at > ~300 Hz for the pellet solution case. The observed difference (~20 times) of the transition frequencies for the stock/supernatant and the pellet cases well corresponds to that of the measured conductance values ($1x10^{-3}$ S of stock and supernatant versus $4x10^{-5}$ S of pellet solution), implying similar values of double layer capacitances. The imaginary part (Im[Y]/ω) shows a transition at much higher frequencies (100 kHz – 1 MHz) than the real part case. This is

because the time constant in this high frequency range involves the liquid capacitance, which is significantly smaller than the double layer capacitance. The Au nanoparticles, as synthesized, are functionalized with surface charges (citrate ions), and may be expected to make a contribution to ionic conduction under RF exposure. The measurement result, however, does not support that possibility, and this can be understood in view of the relatively large mass of Au NPs compared to atomic or molecular level ions.

Presence of background ions in the colloidal solutions were tested by TEM analysis (Fig. 24). Revealed in the TEM image of stock solution are high-contrast Au NPs with uniform size and low-contrast precipitates as indicated by arrows. High-resolution TEM imaging and EDS analysis reveal that those low-contrast precipitates contain NaCl crystalline components and that Na, K, O, and Cl are the dominant elements in the precipitates. The TEM image of the supernatant (not shown here) also reveals NaCl crystalline domains, same as the stock solution case. There was no evidence that Au NPs are contained in the low-contrast precipitates. Overall the TEM analysis confirms presence of low-contrast precipitates in both the stock solution and the supernatant, which originate from the same electrolyte solutions.

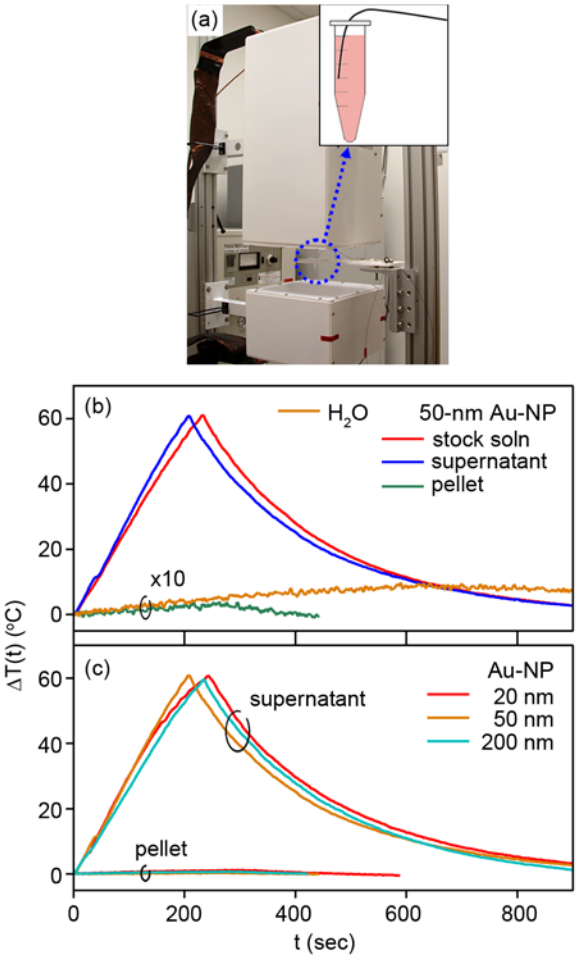

Figure 19. RF heating. (a) Experimental setup; the inset shows a 0.5 mL solution placed in between the electrodes of RF generator. (b) Temperature rise profiles of 50-nm Au-NP solutions (stock, supernatant, and pellet solutions) and DI water (brown); note 10x magnification for both pellet and DI water. (c) Temperature rise profiles of three different particle size solutions (20, 50 and 200 nm: supernatant and pellet solutions).

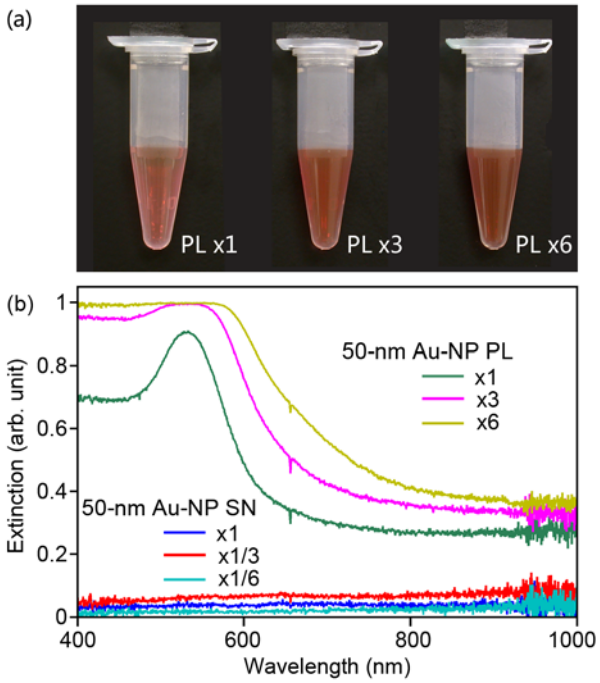

Figure 20. Separation of gold nanoparticles by centrifugation and preparation of supernatants and resuspended pellet solutions at different concentrations. (a) 50-nm Au-NP pellet solutions: x1 (as separated from original stock solution); x3 (3 times higher NP concentration); x6 (6 times higher NP concentration). (b) Extinction spectra of supernatants diluted at three different levels (SN x1, x1/3, x1/6) and three pellet solutions (PL x1, x3, x6).

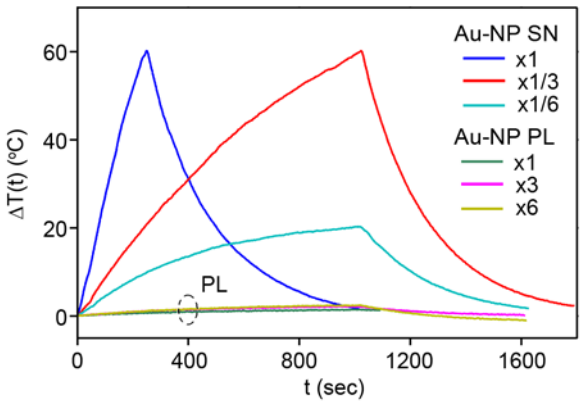

Figure 21. Temperature rise profiles of three supernatants at different dilutions (SN x1, x1/3, x1/6) and three pellet solutions at different Au-NP concentrations (PL x1, x3, x6: bottom curves bundled).

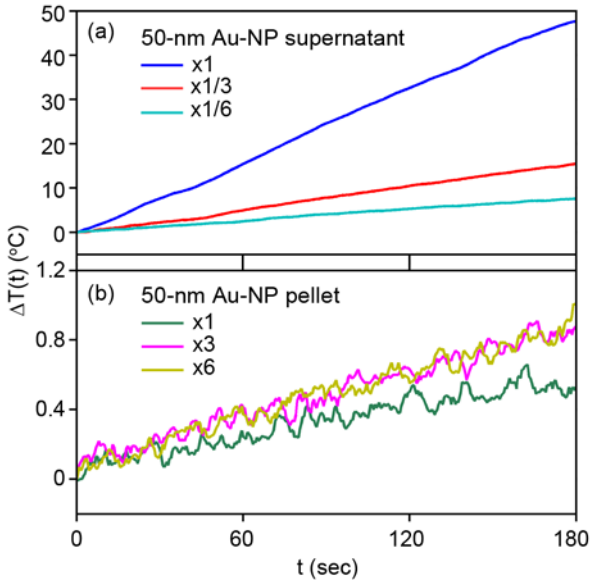

Figure 22. The initial parts of temperature rise profiles. (a) Supernatants (x1, x1/3, x1/6). (b) Pellet solutions (x1, x3, x6).

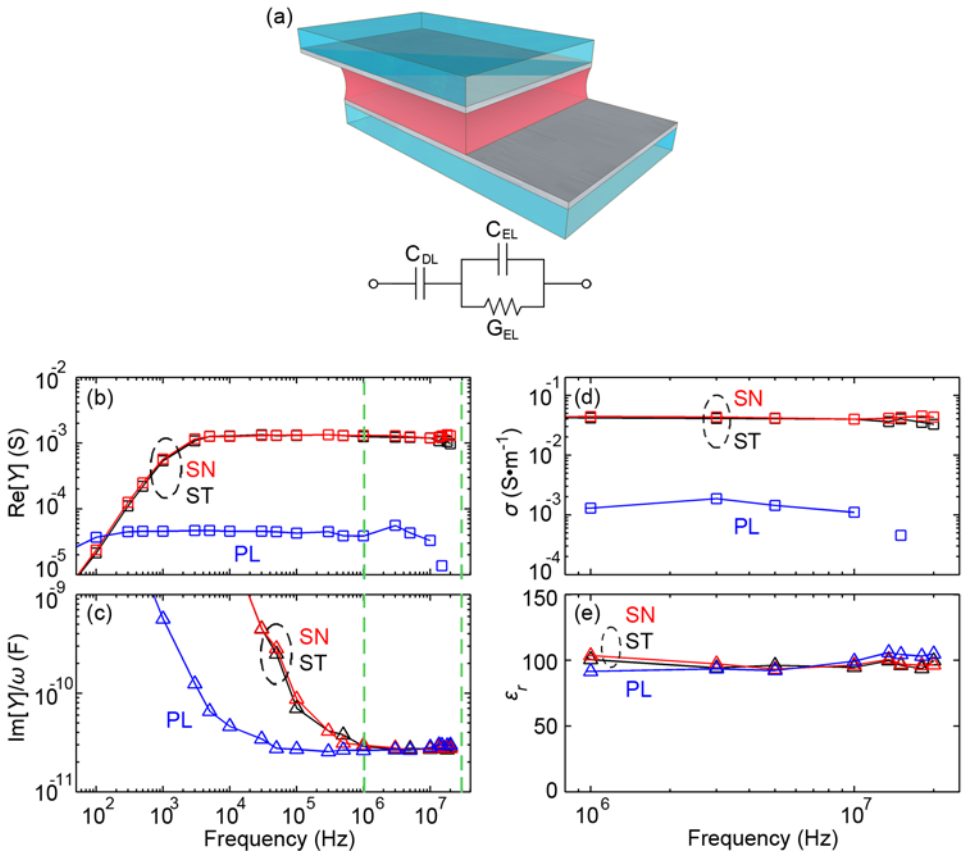

Figure 23. Electrical conductivity and dielectric constant of gold colloidal solutions. (a) a liquid electrolyte cell (dimensions: 4 mm x 4 mm electrode area in the overlapping region and 530 μm gap) and its equivalent circuit model. (b) Admittance spectra of 50-nm Au-NP stock (black curve), supernatant (red) and pellet (blue) solutions. (c) AC conductivity (σ) and dielectric constant (ε_r) of liquid calculated from the flat region in the high frequency range (marked with green dashed lines: 1 MHz – 20 MHz).

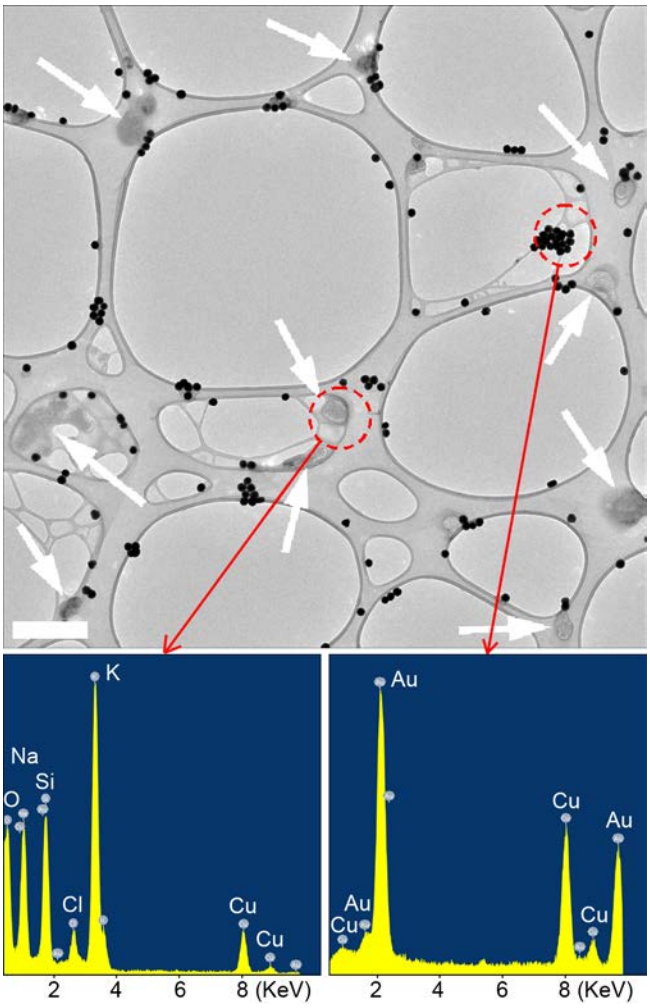

Figure 24. Representative bright-field TEM images (scale bar: 500 nm) and EDS of Au nanoparticles and precipitates from the colloidal solution.

4.3 SUMMARY

This study elucidates the physical mechanisms of heat generation in Au-nanoparticle colloidal solutions induced by RF electromagnetic waves. The possible role of Au nanoparticles in RF heating was systematically investigated by separating the metal nanoparticles away from the colloidal solutions by centrifugation. Contrary to the previously-taken assumption in this field, it is found that Au nanoparticles do not make any measurable contribution to RF energy absorption. The electrical conductivity measurement of the solutions with and without Au nanoparticles reveals that the Joule heating via ionic conduction in the electrolyte solutions is the dominant mechanism of RF-radiation-to-thermal conversion.

There have been reports on microwave heating of Au-NP-containing solutions performed at 1-12 GHz frequency [88, 89, 90]. It is interesting to note that the observed microwave heating of colloidal solutions has been commonly ascribed to induction heating in Au NPs. According to the formula discussed above for induction heating in a non-magnetic metal particle [27], however, the amount of heat generation at microwave frequency is estimated to be negligible, e.g., 10^{-23} W per 20-nm Au-NP at 2.5 GHz and H_0 = 1 A/m. It should also be noted that in those reports [89, 90] the amount of induction heating in a Au NP was incorrectly estimated (overestimated by four orders of magnitude to 10^{-12} W level) referring to an alternative expression derived for a cylindrical body [91, 92]. Considering the ionic nature of the solutions used in those experiments, ionic conduction Joule heating is believed to be the main mechanism of microwave heating observed in their work.

Owing to the versatile and yet unique physical and chemical properties, gold nanoparticles are finding an ever-growing number of applications, e.g., in biomedical area, as agents for labeling, delivery, sensing or heating (photo-thermal conversion). In most

bioapplications, Au NPs operate in an ionic solution ambient, whose ionic nature originates from the intrinsic (electrolyte solutions used for NP synthesis) or extrinsic reasons (biological ambient or buffer solutions used). A clarification reported in this work on the role of Au NPs in RF heating of colloidal solutions suggests that caution needs to be exercised when designing metal NP experiments that involve RF-wave exposure of metal colloidal solutions. Further a clear understanding of the physical mechanism of the RF-wave interaction with metal colloidal solutions is expected to help set a clear potential of the subject phenomenon in developing new applications.

5.0 CONCLUSION AND PROSPECTS

In this thesis, we have investigated interactions of micro/nano particles with electromagnetic waves. The scope of this study includes design, fabrication and characterization of metal nano-optic structures for optical trapping, and investigation of heating effect of gold nanoparticles in the presence of radiofrequency radiation.

Optical trapping by use of a metal thin-film structure has been achieved with two types of structures. In the metallic nanoslit array structure, an incident light transmits through each slit involving a series of surface plasmon interactions, i.e., excitation, propagating and coupling to radiation modes. The transmitted field distribution is numerically analyzed. The structural and materials parameters are adjusted and optimized in order to shape the transmitted beam into a proper shape desirable for optical trapping. A 7-slit array with 250-nm slit spacing and 40-nm slit width was designed, fabricated and tested. The escape forces of the nanoslit array lens are measured to be ~0.07 pN at 32 mW incident laser power.

In the case of Au/Cr metal edge structure, an incident light is diffracted around the edge, producing a localized intensity distribution of light around the gold film edge. We developed a model based on ray optics and calculated the optical forces that a microsphere would experience in the diffraction fields. It is found that a microsphere can be trapped around this metal edge. The lateral confinement is ascribed to the localized intensity distribution and the vertical confinement is mainly due to the balance of gravity, buoyancy and upward optical scattering forces. The role

of a semitransparent Cr thin film is investigated. It is found that a Cr thin film helps reduce the upward scattering force while enhancing the lateral intensity gradient. Application of the metal edge trapping is demonstrated in two ways. Multiple trapping by a patterned Au/Cr thin film edge structure is tested. A dual-trap system formed by two on-chip-integrated traps, with each associated with a micro-bead biologically linked with microtubules, is presented. A potential use of this system to study biological processes is discussed. Size-selective trapping of microspheres by the metal edge trap is also demonstrated.

In this thesis, we also investigated the heating effect of gold nanoparticle colloids in the presence of RF electromagnetic wave. We quantitatively measured heat generation in Au-nanoparticle colloidal solutions induced by RF waves (13.56 MHz; 25 W). The possible role of Au nanoparticles in RF heating is systematically investigated by separating the metal nanoparticles away from the colloidal solutions by centrifugation. Contrary to the previously-taken assumption in this field, it is found that Au nanoparticles do not contribute to RF energy absorption. The electrical conductivity measurement of the solutions with and without Au nanoparticles reveals that the Joule heating via ionic conduction in the electrolyte solutions is the dominant mechanism of RF-radiation-to-thermal conversion.

In the future, at least two relevant topics are suggested for further study. First, the dual-trap system that is formed by patterned metal edges and is associated with micro-microspheres biologically linked with microtubules provides a promising scaffold to develop artificial spindles for the study of biological processes of cells. In order to find practical usage, the trapping performance would need to be quantitatively measured and calibrated, e.g., establish the linear relationship of displacement and restoring force. Second, the RF experiment of Au NP colloids clearly shows that Au nanoparticles do not contribute to RF energy absorption; instead, ionic

conduction in the electrolyte solutions plays the role in Joule heating. While this study unequivocally demonstrates negligible effect of Au NPs in RF-energy absorption, it is not known yet whether presence of Au-NPs would significantly alter the thermal transport properties. During RF exposure, Au NPs may aggregate and form clusters/assemblies around the target area. It will be interesting to study whether these densely-populated Au-NPs can alter the thermal capacity/transport properties of the local medium therefore amplify the local temperature change during RF heating.

BIBLIOGRAPHY

[1] Ashkin, A. Acceleration and trapping of particles by radiation pressure. *Phys. Rev. Lett.* **24**, 156-59 (1970).

[2] Ashkin, A. Forces of a single-beam gradient laser trap on a dielectric sphere in the ray optics regime. *Biophys. J.* **61**, 569-582 (1992).

[3] Harada, Y. & Asakura, T. Radiation forces on a dielectric sphere in the Rayleigh scattering regime. *Opt. Commun.* **124**, 529-541 (1996).

[4] Rohrbach, A. & Stelzer, E. H. K. Trapping Forces, force constants, and potential depths for dielectric spheres in the presence of spherical aberrations. *Appl. Opt.* **41**, 2494-2507 (2002).

[5] Neuman, K. C. & Block, S. M. Optical trapping. *Rev. Sci. Instrum.* **75**, 2787-2809 (2004).

[6] Grier, D. G. A revolution in optical manipulation. *Nature (London)* **424**, 810-816 (2003).

[7] Pissuwan, D., Valenzuela, S. M. & Cortie, M. B. Therapeutic possibilities of plasmonically heated gold nanoparticles. *Trends Biotechnol.* **24**, 62-67 (2006).

[8] Huang, X. H., El-Sayed, I. H., Qian, W. & El-Sayed, M. A. Cancer cell imaging and photothermal therapy in the near-infrared region by using gold nanorods. *J. Am. Chem. Soc.* **128**, 2115-2120 (2006).

[9] Richardson, H. H., Hickman, Z., Govorov, A. O. Thomas, A. & Zhang, W. Thermooptical Properties of Gold Nanoparticles Embedded in Ice: Characterization of Heat Generation and Melting. *Nano Lett.* **6**, 783-788 (2006).

[10] Gobin, A. M., O'Neal, D.P., Halas, N. J. & West, J. L. Near infrared laser-tissue welding using nanoshells as an exogenous absorber. *Lasers Surg. Med.* **37**, 123-129 (2005).

[11] Govorov, A. O. & Richardson, H. H. Generating heat with metal nanoparticles. *Nanotoday* **2**, 30-38 (2007).

[12] Kreibig, U. & Vollmer, M. *Optical Properties of Metal Clusters* (Springer, Berlin, 1995).

[13] Bohren, C. F. & Huffman, D. R. Absorption and Scattering of Light by Small Particles, (Wiley, New York, 1983).

[14] Link, S. & El-Sayed, M. A. Shape and size dependence of radiative, non-radiative and photothermal properties of gold nanocrystals. *Int. Rev. Phys. Chem*. **19**, 409-453 (2000)

[15] Boyer, D., Tamarat, P., Maali, A., Lounis, B. & Orrit, M. Photothermal imaging of nanometer-sized metal particles among scatterers, *Science* **297**, 1160-1163 (2002).

[16] Hu, M. & Hartland, G. V. Heat dissipation for Au particles in aqueous solution: relaxation time versus size. *J. Phys. Chem. B* **106**, 7029-7033 (2002).

[17] Pitsillides, C. M., Joe, E. K., Wei, X., Anderson, R. R. & Lin, C. P. Selective cell targeting with light-absorbing microparticles and nanoparticles. *Biophys. J.* **84**, 4023-4032 (2003).

[18] Hirsch, L. R., Stafford, R. J., Bankson, J. A., Sershen, S. R., Rivera, B., Price, R. E., Hazle, J. D., Halas, N. J. & West, J. L. Nanoshell-mediated near-infrared thermal therapy of tumors under magnetic resonance guidance. *Proc. Natl. Acad. Sci. U. S. A.* **100**, 13549-13554 (2003).

[19] Govorov, A. O., Zhang, W., Skeini, T., Richardson, H., Lee, J. & Kotov, N. A., Gold nanoparticle ensembles as heaters and actuators: melting and collective plasmon resonances. *Nanoscale Res. Lett.* **1**, 84-90 (2006).

[20] Skirtach, A. G., Dejugnat, C., Braun, D., Susha, A. S., Rogach, A. L. Parak, W., Möhwald, H. & Sukhorukov, G. B. The role of metal nanoparticles in remote release of encapsulated materials. *Nano Lett.* **5**, 1371-1377 (2005).

[21] Gannon, C. J., Patra, C. R., Bhattacharya, R., Mukherjee, P. & Curley, S. A. Intracellular gold nanoparticles enhance non-invasive radiofrequency thermal destruction of human gastrointestinal cancer cells. *J. Nanobiotechnol*. **6**, doi:10.1186/1477-3155-6-2 (2008).

[22] Cardinal, J., Klune, J. R., Chory, E., Jeyabalan, G., Kanzius, J. S., Nalesnik, M. & Geller, D. A. Non-invasive radiofrequency ablation of cancer targeted by gold nanoparticles. *Surgery* **144**, 125-132 (2008).

[23] Curley, S. A., Cherukuri, P., Briggs, K., Patra, C. R., Upton, M., Dolson, E. & Mukherjee, P. Noninvasive radiofrequency field induced hyperthermic cytotoxicity in human cancer cells using cetuximab-targeted gold nanoparticles. *J. Exp. Ther. Oncol***. 7**, 313-326 (2008).

[24] Moran, C. H., Wainerdi, S. M., Cherukuri, T. K., Kittrell, C., Wiley, B. J., Nicholas, N. W., Curley, S. A., Kanzius, J. S. & Cherukuri, P. Size-dependent joule heating of gold nanoparticles using capacitively coupled radiofrequency fields. *Nano Res.* **2**, 400-405 (2009).

[25] Dalal, R. V., Larson, M. H., Neuman, K. C., Gelles, J., Landick, R. & Block, S. M. Pulling on the nascent RNA during transcription does not alter kinetics of elongation or ubiquitous pausing. *Mol. Cell.* **23**, 231–239 (2006).

[26] Visscher, K., Schenitzer, M. J. & Block, S. M. Single kinesin molecules studied with a molecular force clamp. *Nature* **400**, 184-189 (1999).

[27] Decastro, M. J., Fondecave, R. M., Clarke, L. A., Schmidt, C. F. & Stewart, R. J. Working strokes by single molecules of the kinesin-related microtubule motor ncd. *Nat. Cell Biol.* **2**, 724-729 (2000)

[28] Kerssmemakers, J. W. J., Janson, M. E., Van Der Horst, A., Dogterom, M., Optical trap setup for measuring microtubule pushing forces, *Appl. Phys. Lett.* **83**, 4441-4443 (2003)

[29] Grishchuk, E. L., Molodtsov, M. I., Ataullakhanov, F. I., Mcintosh, J. R., Force production by disassembling microtubules, *Nature* **438**, 384-388 (2005)

[30] Jackson, J. D. *Classical electrodynamics*. 3rd ed. (Wiley, New York, 1999)

[31] Goldman, A. J., Cox, R. G. & Brenner, H. Slow viscous motion of a sphere parallel to a plane wall—I Motion through a quiescent fluid. *Chem. Engng. Sci.* **22**, 637-651 (1967).

[32] Soni, G. V., Hameed, F. M., Roopa, T. & Shivashankar, G. V. Development of an optical tweezer combined with micromanipulation for DNA and protein nanobioscience. *Curr. Sci. 83,* 1464-1470 (2002).

[33] Capitanio, M., Romano, G., Ballerini, R., Giuntini, M. & Pavone, F. S. Calibration of optical tweezers with differential interference contrast signals. *Rev. Sci. Instrum.* **73**, 1687-1696 (2002).

[34] Grier, D. G. A revolution in optical manipulation. *Nature (London)* **424**, 810-816 (2003).

[35] Sun, Z. J. & Kim, H. K. Refractive transmission of light and beam shaping with metallic nano-optic lenses. *Appl. Phys. Lett.* **85**, 642-644 (2004).

[36] Landau, L.D., Lifshits, E.M. & Pitaevskii, L.P. *Electrodynamics of Continuous Media*, 2nd ed. (Pergamon, New York, 1984).

[37] Rybakov, K.I., Semenov, V.E., Egorov, S.V., Eremeev, A.G., Plotnikov, I.V. & Bykov, Y.V. Microwave heating of conductive powder materials, *J. Appl. Phys.* **99**, 023506-023506-9 (2006).

[38] Ignatenko, M., Tanaka, M. & Sato, M. Absorption of microwave energy by spherical nonmagnetic metal particle, *Jpn. J. Appl. Phys.* **48**, 067001-067001-2 (2009).

[39] Goldenberg, H. & Tranter, G. J. Heat flow in an infinite medium heated by a sphere. *Br. J. Appl. Phys.* **3**, 296-298 (1952).

[40] Xia, Y. N. & Halas, N. J. Shape-controlled synthesis and surface plasmonic properties of metallic nanostructures. *MRS Bull.* **30**, 338-344 (2005).

[41] Shuba, M. V., Slepyan, G. A., Maksimenko, S. A. & Hanson, G. W. Radiofrequency field absorption by carbon nanotubes embedded in a conductive host. *J. Appl. Phys*. **108,** 114302-114302-10 (2010).

[42] Palpant, B., Guillet, Y., Rashidi-Huyeh, M. & Prot, D. Gold nanoparticle assemblies: Thermal behaviour under optical excitation. *Gold Bull.* **41**, 105-115 (2008).

[43] Pramanik, M., Swierczewska, M., Green, D., Sitharaman, B. & Wang, L. V. Single-walled carbon nanotubes as a multimodal-thermoacoustic and photoacoustic-contrast agent. *J. Biomed. Opt.* **14**, 034018 (2009).

[44] De la Zerda, A., Zavaleta, C., Keren, S., Vaithilingam, S., Bodapati, S., Liu, Z., Levi, J., Smith, B. R., Ma, T. J., Oralkan, O., Cheng, Z., Chen, X., Dai, H., Khuri-Yakub, B. T. & Gambhir, S. S. Carbon nanotubes as photoacoustic molecular imaging agents in living mice. *Nat. Nanotechnol*. **3**, 557-562 (2008).

[45] Kerssemakers, J. W. J., Janson, M. E., Van Der Horst, A. & Dogterom, M. Optical trap setup for measuring microtubule pushing forces. *Appl. Phys. Lett.* **83**, 4441-4443 (2003)

[46] Palik, E. D. ed., *Optical Constants of Solids*. (Academic Press, New York, 1998).

[47] Sun, Z. J., Jung, Y. S. & Kim, H. K, Role of surface plasmons in the optical interaction in metallic gratings with narrow slits. *Appl. Phys. Lett*, **83**, 3021 (2003)

[48] Ashkin, A., Dziedzic, J. M., Bjorkholm, J. E. & Chu, S. Observation of a single-beam gradient force optical trap for dielectric particles. *Opt. Lett.* **11**, 288-290 (1986).

[49] Block, S. M., Goldstein, L. S. B. & Schnapp, B. J. Bead movement by single kinesin molecules studied with optical tweezers. *Nature* **348**, 348 - 352 (1990).

[50] Applegate, Jr., R. W., Squier, J., Vestad, T., Oakey J. & Marra, D. W. M. Fiber-focused diode bar optical trapping for microfluidic flow manipulation. *Appl. Phys. Lett.* **92**, 013904 (2008).

[51] Mio, C., Gong, T., Terray, A. & Marr, D. W. M. Design of a scanning laser optical trap for multiparticle manipulation. *Rev. Sci. Instrum.* **71**, 2196-2201 (2000).

[52] Oakey, J., Allely, J. & Marr, D. W. M. Laminar Flow-Based Separations at the Microscale. *Biotechnol. Prog.* **81**, 1439-1442 (2002).

[53] Terray, A., Oakey, J. & Marr, D. W. M., Microfluidic Control Using Colloidal Devices. *Science* **296**, 1841-1844 (2002).

[54] Dufresne, E. R., Spalding, G. C., Dearing, M. T., Sheets, S. A. & Grier, D. G. Computer generated holographic optical tweezer arrays. *Rev. Sci. Instrum.* **72**, 1810-1816 (2001).

[55] Blakely, J. T., Gordona R. & Sinton, D. Flow-dependent optofluidic particle trapping and circulation. *Lab Chip* **8**, 1350–1356 (2008).

[56] Schonbrun, E., Rinzler, C. & Croziera, K. B. Microfabricated water immersion zone plate optical tweezer. *Appl. Phys. Lett.* **92**, 071112 (2008).

[57] Righini, M., Zelenina, A. S., Girard C. & Quidant, R. Parallel and selective trapping in a patterned plasmonic landscape. *Nature Phys.* **3**, 477-480 (2007).

[58] Wang, K., Schonbrun, E., Steinvurzel P. & Crozier, K. B. Scannable Plasmonic Trapping Using a Gold Stripe. *Nano Lett.* **10**, 3506-3511 (2010).

[59] Tlusty, T., Meller A. & Bar-Ziv, R. Optical Gradient Forces of Strongly Localized Fields. *Phys. Rev. Lett.* **81**, 1738-1741 (1998).

[60] Walz J.Y. & Prieve, D.C. Prediction and Measurement of the Optical Trapping Forces on a Microscopic Dielectric Sphere. *Langmuir* **8**, 3073-3082 (1992).

[61] Simmons, R. M., Finer, J. T., Chu S. & Spudich, J. A. Quantitative Measurements of Force and Displacement Using an Optical Trap. *Biophys. J.* **70**, 1813-1822 (1996).

[62] Bormuth, V., Jannasch, A., Ander, M., van Kats, C. M., van Blaaderen, A., Howard, J. & Schaffer, E. Optical trapping of coated microspheres. *Opt. Express* **16**, 13831-13844 (2008).

[63] Piazza, R. Thermophoresis: moving particles with thermal gradients. *Soft Matter* **4**, 1740-1744 (2008)

[64] Piazza R. & Parola, A. Thermophoresis in colloidal suspensions. *J. Phys.: Condens. Matter* **20**, 153102-18 (2008)

[65] Inoué, S. & Salmon, E. D. Force Generation by Microtubule Assembly/Disassembly in Mitosis and Related Movements. *Mol. Biol. Cell* **6**, 1619–1640 (1995).

[66] Dogterom, M. & Yurke B. Measurement of the force-velocity relation for growing microtubules. *Science* **278**, 856-860 (1997).

[67] Howard, J. & Hyman, A. A. Dynamics and mechanics of the microtubule plus end. *Nature* **422**, 753-758 (2003).

[68] Holy, T. E., Dogterom, M., Yurke, B. & Leibler, S. Assembly and positioning of microtubule asters in microfabricated chambers. *Proc. Natl. Acad. Sci.* **94**, 6228-6231 (1997).

[69] Kapitein, L. C., Peterman, E. J. G., Kwok, B. H., Kim, J. H., Kapoor, T. M. & Schmidt, C. F. The bipolar mitotic kinesin Eg5 moves on both microtubules that it crosslinks. *Nature* **435**, 114-118 (2005).

[70] Valentine, M. T., Fordyce, P. M., Krzysiak, T. C., Gilbert, S. P. & Block, S. M. Individual dimmers of the mitotic kinesin motor Eg5 step processively and support substantial loads in vitro. *Nature cell Biol.* **8**, 470-476 (2006).

[71] Valentine, M. T. & Gilbert, S. P. To step or not to step? How biochemistry and mechanics influence processivity in Kinesin and Eg5. *Curr. Opin. Cell Biol.* **19**, 75-81 (2007).

[72] Alberts, B. *Molecular Biology of the Cell*. 4th ed. (Garland Science, New York, 2002)

[73] Helenius, J., Brouhard, G., Kalaidzidis, Y., Diez, S. & Howard, J. The depolymerizing kinesin MCAK uses lattice diffusion to rapidly target microtubule ends. *Nature* **441**, 115-119 (2006).

[74] Eastman, J. A., Phillpot, S. R., Choi, S. U. S. & Keblinski, P. Thermal transport in nanofluids. *Annu. Rev. Mater. Res.* **34**, 219-246 (2004).

[75] Johnson, C. C. & Guy, A. W. Non-ionizing electromagnetic wave effects in biological materials and systems. *Proc. IEEE* **60**, 692-718 (1972).

[76] Klune, J. R., Jeyabalan, G., Chory, E. S., Kanzius, J. & Geller, D. A. Pilot investigation of a new instrument for non-invasive radiofrequency ablation of cancer. *J. Surg. Res.* **137**, 263 (2007).

[77] Data sheet of gold nanoparticle colloidal solutions, Ted Pella, Inc.; http://www.tedpella.com/gold_html/goldsols.htm

[78] Kanzius, J. S. U.S. Patent Publication Nos. US 2006/0190063 A1, US 2005/02511233 A1, US 2005/0251234 A1, and World Intellectual Property Organization WO 2007/027614.

[79] Ambrus, J. H., Moynihan, C. T. & Macedo, P. B. Conductivity relaxation in a concentrated aqueous electrolyte solution. *J. Phys. Chem.* **76**, 3287 (1972).

[80] Turkevich, J., Stevenson, P.C. & Hillier, J. A study of the nucleation and growth processes in the synthesis of colloidal gold. *Discuss. Faraday. Soc.* **11**, 55-75 (1951).

[81] Frens, G. Controlled nucleation for the regulation of the particle size in monodisperse gold suspensions. *Nature Phys. Sci.* **241**, 20-22 (1973).

[82] Hackley, V. Nanoparticle standards at NIST: Gold nanoparticle reference materials and their characterization (RM 8011-8013); https://srmors.nist.gov/orderingSRMs.cfm

[83] Lide, D. R. ed., *CRC Handbook of Chemistry and Physics*, 87th ed. (Taylor & Francis, New York, 2006) p. 6-2, p. 6-15 & p. 12-39

[84] Carslaw, H. S. & Jaeger, J. C. *Conduction of Heat in Solids* (Oxford, New York, 1959).

[85] Considering that both stock and supernatant solutions show the same heating rate and that relatively low concentrations of solute and NPs are introduced to water, the heat capacity of the aqueous solutions (with or without Au-NP) is assumed to remain unchanged from that of water.

[86] Robinson, R. A. & Stokes, R. H. *Electrolyte Solutions*, 2nd ed. (Butterworths, London, 1959).

[87]The accuracy of impedance measurement with this setup degrades at the high frequency end: note the rapid falloff of the PL curve at ~20 MHz in Fig. 6b. Also, the chemical resistance of aluminum may not be as good as that of gold, and the aluminum films (200 nm thick) may form an oxide layer over time. Presence of a thin dielectric layer on electrode surface can affect the double layer capacitance. The effect of the interfacial layer capacitances associated with electrodes, however, becomes negligible in the high frequency regime (> 1 MHz: See Fig. 6c). Overall the valid range of extracting AC conductivity and dielectric constant with this setup is considered to be 1 MHz – 10 MHz.

[88] Hamad-Schifferil, K., Schwartz, J. J., Santos, A.T., Zhang, S. & Jacobson, J. M. Remote electronic control of DNA hybridization through inductive coupling to an attached metal nanocrystal antenna. *Nature* **415**, 152-155 (2002).

[89] Kogan, M. J., Bastus, N. G., Amigo, R., Grillo-Bosch, D., Araya, E., Turiel, A., Labarta, A., Giralt, E. & Puntes, V.F. Nanoparticle-mediated local and remote manipulation of protein aggregation, *Nano Lett.* **6**, 110-115 (2006).

[90] Aslan, K. & Geddes, C. D. Microwave-Accelerated Ultra-Fast Nanoparticle Aggregation Assays using Gold Nanoparticles. *Anal. Chem.* **79**, 2131-2136 (2007).

[91] Orfeuil, M. *Electric Process Heating* (Battelle Press, Columbus, OH, 1987).

[92] In References 32 and 33 (see supporting information therein), the microwave heating of a Au NP was estimated referring to the following formula taken from Ref. 34 (page 405): $4\pi\mu_0 fF\frac{d_0}{d}H_0^2$, where f is the frequency, and F is a power transmission factor depending on the ratio of cylinder diameter (d) to skin depth (d_0) of metal. Their estimation is flawed because the power transmission F was erroneously read (it should be read at $d/d_0 = 1/80$, not 80), causing the induction heating amount overestimated by four orders of magnitude.